Master's Thesis

ELECTRIC-THERMAL PHOTOVOLTAIC MODELING AND APPLICATIONS

Xuan Hung Mai

Department of Electrical Engineering

Graduate School of UNIST

2017

ELECTRIC-THERMAL PHOTOVOLTAIC MODELING AND APPLICATIONS

Xuan Hung Mai

Department of Electrical Engineering

Graduate School of UNIST

ELECTRIC-THERMAL PHOTOVOLTAIC MODELING AND APPLICATIONS

A thesis
submitted to the Graduate School of UNIST
in partial fulfillment of the
requirements for the degree of
Master of Science

Xuan Hung Mai

12. 15. 2016
Approved by

_____

Advisor
Katherine Ann Kim

ELECTRIC-THERMAL PHOTOVOLTAIC MODELING AND APPLICATIONS

Xuan Hung Mai

This certifies that the thesis of Xuan Hung Mai is approved.

12. 15. 2016

_____
Advisor: Katherine Ann Kim

_____
Jee Hoon Jung

_____
Jingook Kim

ABSTRACT

This work introduces an electric-thermal model for a photovoltaic (PV) cell, which combines electrical and thermal parameters and also incorporates dynamic characteristics and accurate modeling in the reverse-bias region. Incoming irradiance and ambient temperature are used to calculate the PV cell temperature based on a five-layer thermal model. The cell temperature in the electrical model is updated according to the thermal model to accurately adjust the PV cell output electrical characteristics. To test and validate the electrical and thermal characteristics of the PV cell, a custom setup was built that allows temperature measurement at the PV cell and glass surfaces. Performance of the electric-thermal model in both forward and reverse-bias region is verified using experimental data in realistic scenarios. This PV model can be scaled up and used to simulate PV systems in a wide variety of applications, extreme environmental conditions, and fault conditions.

Contents

LIST OF FIGURES

LIST OF TABLES

EXPLANATION OF TERMS AND ABBREVIATIONS

Symbol	Meaning
G	Irradiance [W/m^2]
T	Temperature [K]
M	Air mass coefficient
Ipv	PV current [A]
Vpv	PV voltage [V]
K	Boltzmann constant [J/K]
Q	Electron charge [C]
Gn	Nominal irradiance [W/m2]
Tn	Nominal temperature [K]
Mn	Nominal air mass coefficient
Iscn	Nominal short circuit current [A]
Vocn	Nominal open circuit voltage [V]
Impp	Maximum power point current [A]
Vmpp	Maximum power point voltage [V]
Ki	Current temperature coefficient [A/K]
Kv	Voltage temperature coefficient [V/K]
Ns	Number of cells in series
Rs	Series resistance [Ohm]
Rshn	Nominal shunt resistant [Ohm]
Ls	Series inductance [H]
α	Diode ideality factor
Vbd	Breakdown voltage [V]
Isr	Reverse saturation current
Kr	Reverse breakdown scalar coefficient
Cj0	Zero-bias junction capacitance [F]
Φ0	Zero-bias junction potential [V]
T	Mean carrier lifetime [s]
tbd	Breakdown mean carrier lifetime [s]

CHAPTER 1
INTRODUCTION

Among all the clean energy sources, solar photovoltaic (PV) energy has proven to serve an important role in reducing fossil fuel usage. As PV systems become larger and more complex with many different configurations, simulations are needed to analyze PV systems and evaluate new technologies, such as PV control algorithms or power conditioning converter systems [1]. Real-time simulation is an important tool that has the capability to test and simulate PV systems through emulation rather than costly experimental setups [2], [3], [4], [5], [6]. PV system simulation in real time allows the PV model to interface with power converter hardware, called power hardware-in- the-loop simulation (PHILS), which is further explored in this work. For these emulated systems to be effective, the PV models must be accurate. Work in [7], [8] implemented real-time simulation using a simple model based on the single diode PV model. This work further improves the PV model with the goal of real-time simulation using PHILS.

The conventional single-diode PV model is commonly chosen for its simplicity in simulating and calculating PV characteristics in the forward-biased voltage region [9], [10], [11], [12], [13]. However, the singe-diode model lacks dynamic and reverse-bias characteristics, as well as thermal aspects. For applications like PV cells in space or PV concentrators, where the PV system performance heavily relies on temperature, it is important to accurately predict the PV cell temperature. Thus, in order to more fully model a PV cell using real time simulation, the single-diode model can be enhanced to incorporate dynamic characteristics, accurate electric-thermal performance, and fast processing time. Work in [14] introduced a PV model with nonlinear dynamic characteristics in both the forward- and reverse-bias regions, which showed high accuracy under normal illumination, but performance under varied PV temperature was not covered.

Parallel capacitive and series inductive components are included to achieve dynamic cell characteristics. Reverse-bias and breakdown features are also included to accurately capture the reverse-bias breakdown behavior, which is important for modeling certain PV faults [15], [16]. Thermal characteristics of the cell and heat transfer among layers surrounding the cell are used to determine the cell temperature, which affects the PV electrical characteristics and resulting output power. Work in [17] investigated heat transfer between the PV cell and its surrounding layers, but did not account for other PV panel components, such as the glass layer. In this paper, a five layer electric-

thermal model incorporating a single crystalline PV cell is developed and validated using experimental results. The verified model is tested with a PHILS system to check the accuracy of the emulated PV panels.

The PV emulation system operates in two main modes: off-line simulation and PHILS. The off-line simulation has no connection to hardware and is not run in real time. It is used to check the accuracy of the PV model compared to measurements from a PV cell. For PHILS, the setup is connected to hardware and computations for the model are run in real time. The model outputs drive the operation of a power supply that is connected to a hardware device. Measurements of the power supply are fed back to the simulation in real-time to update the model values. This mode is used for dynamic tests, where the dynamic performance of the emulated PHILS PV cell is compared to experimental PV cell measurements. Using the PHILS system, the PV model can be simulated under various load variations with power converter hardware in real-time [18], [19]. Experimental tests can be conducted for not only normal conditions, but also extreme temperature and fault conditions using PHILS. Experimental PV setups that could be dangerous, expensive or time consuming can be realistically emulated using the PHILS system, which allows for fast and cost-effective hardware prototyping.

In this work, a comprehensive electric-thermal PV model is proposed for PHILS applications using a real-time simulator. The model consists of a dynamic electrical PV model and five-layer thermal model, which are integrated together. All equations for the model are outlined and the performance of the electric-thermal PV model is verified with a 1.3-W PV cell tested in a custom testing setup. Static operation is verified using off-line simulation and compared to experimental results. In addition, dynamic operation is verified using the PHILS system connected to a programmable electronic load that generates various load changes and can also perform MPPT.

1.1 The Sun Radiation

The solar system includes the Sun and everything which orbits around it: the Earth, eight other planets, asteroids, and comets. The distance between the Sun and the Earth is approximately 150 million kilometers and it varies slightly throughout the year, mainly for the reason that the Earth's orbit is an ellipse and not a perfect circle.

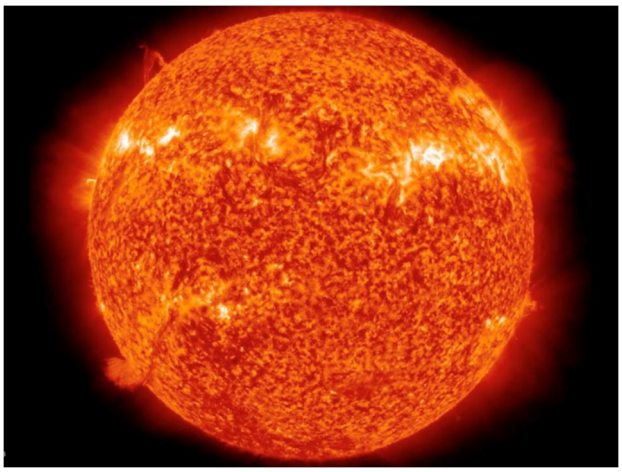

Figure 1: The sun seen from outside [32]

The Sun is not the hottest or coolest star, or intrinsically the brightest or faintest. However, because by distance, it is the closest star to the Earth, it is seen in our sky to be bigger and brighter than any other star. The Sun's diameter is about 1.4 million kilometers, hence it would take 110 Earths strung together to be equal to the diameter of the Sun. The Sun mostly contains hydrogen which about 92.1% of the number of atoms and 75% of its mass. Helium can also be found in the Sun which 7.8% of the number of atoms and 25% of its mass. Other 0.1% contains heavier elements, mainly carbon, nitrogen, oxygen, neon, magnesium, silicon and iron. The Sun is neither a solid nor gas but in fact it is actually plasma which is tenuous and gaseous at the surface, but it is denser down near the Sun's fusion core [1].

The type of star like the Sun can shine for nine to ten billion years. The Sun has existed for 4.5 billion years, judging by the age of moon rocks. From this information, astrophysical suggests a theory that the Sun will turn into a red giant star in about five billion years [2].

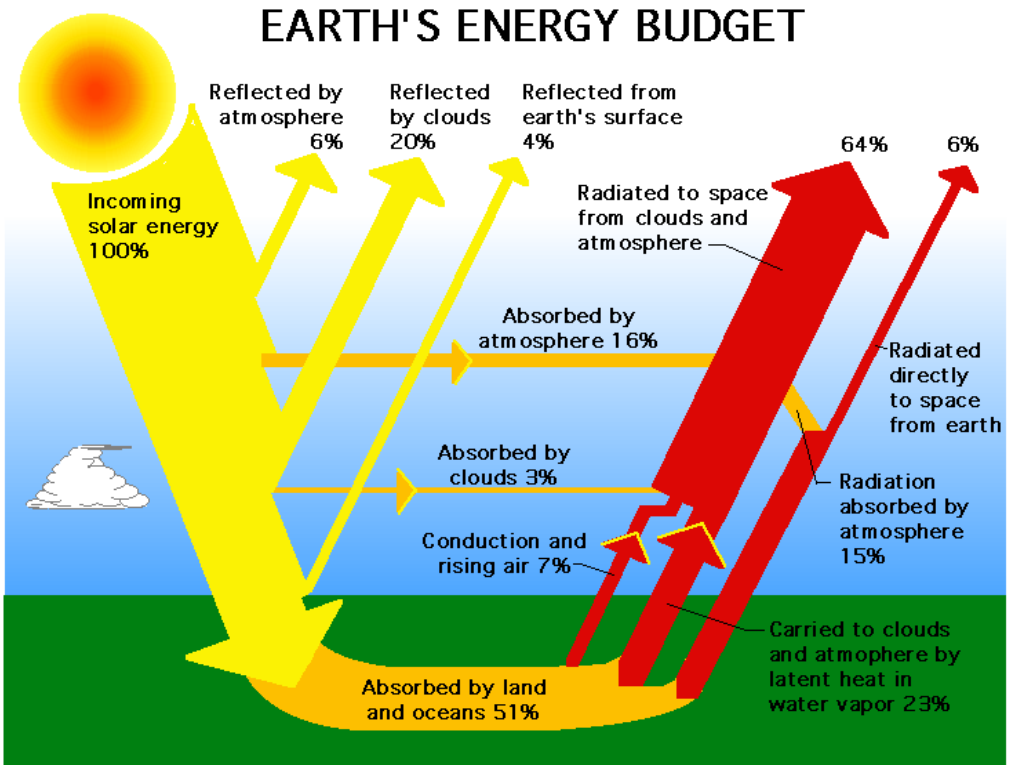

Figure 2: Earth's energy budget [33]

There is an enormous energy continuously emitted from the sun dispersing into outer space in all directions. There is only a small amount of this energy that reach the earth and other planets.

While passing through outer space, which is characterized by vacuum, there are different types of solar energy which remain intact and are not changed until the radiation reaches the top of the earth's atmosphere. In outer space, there are many types of radiation, which are: gamma ray, X-ray, ultraviolet, and infrared radiations [3].

The total energy entering the Earth's atmosphere is approximately 174 petawatts, in which a pet watt is 10 exponential 15 joules per second. This consists of:

- Solar radiation (99.978%, or nearly 174 petawatts; or about 340 W/m^2)
    - This is equal to the product of the solar constant, about 1366 watts per square meter, and the area of the Earth's disc as seen from the Sun, about 1.28×10^{14} square meters, averaged over the Earth's surface, which is four times larger. The solar flux averaged over just the sunlit half of the earth's surface is about 680 W/m^2
- Geothermal energy (0.013%, or about 23 terawatts; or about 0.045 W/m^2)
    - This is produced by stored heat and heat produced by radioactive decay leaking out of the Earth's interior.
- Tidal energy (0.002%, or about 3 terawatts; or about 0.0059 W/m^2)
    - This is produced by the interaction of the Earth's mass with the gravitational fields of other bodies such as the Moon and Sun.
- Waste heat from fossil fuel consumption (about 0.007%, or about 13 terawatts; or about 0.025 W/m^2)

One thing to note is that the solar constant varies by about 0.1% over a solar cycle and it is not guaranteed to be within one watt per square meter. Hence geothermal and tidal energy contributions are less than the uncertainty in the total solar power.

The average reflectivity of the Earth is about 0.3, i.e. 30% of the incoming solar irradiance is reflected back into outer space, while 70% is absorbed by the Earth and reradiated as infrared. Our planet's reflectivity varies depending on the time in a year, but 0.3 is the average value. It also varies strongly spatially: ice sheets have a high reflectivity, while the oceans is pretty low. The contributions of geothermal and tidal energy sources are so small that they are omitted from the following calculations. The 30% of the incoming energy is **reflected**, which includes:

- 6% reflected by the atmosphere
- 20% reflected by clouds
- 4% reflected by the ground (including land, water and ice)

The remaining 70% of the incoming energy is **absorbed**:

- 51% is absorbed by ground and water, then emerging in the following ways:
    - 23% transferred back to the atmosphere through latent heat by the evaporation of water

- 7% transferred back to the atmosphere through heated rising air
- 6% radiated directly into space
- 15% transferred to the atmosphere by radiation, then reradiated into space

- 19% absorbed by the atmosphere and clouds, which includes:
  - 16% reradiated back into space
  - 3% transferred to clouds, from where it is radiated back into space

While the Earth is at thermal equilibrium, the same 70% that is absorbed will be **reradiated**:

- 64% by the clouds and atmosphere
- 6% by the ground [4]

1.2 Structure of a PV Cell

Photovoltaic (PV) cells are commonly made from at least 2 semi-conductor layers. One layer is a positive charge, the other is a negative charge. Sunlight contains photons which is the source of solar energy. When PV cell is exposed to sunlight, photons are reflected, passing through, or absorbed by the solar cell. When the negative layer of the photovoltaic cell absorbed enough photons, electrons are freed from the negative semiconductor material. Because of the manufacturing process of the positive layer, these freed electrons move to the positive layer, thus creating a voltage differential, similar to a battery.

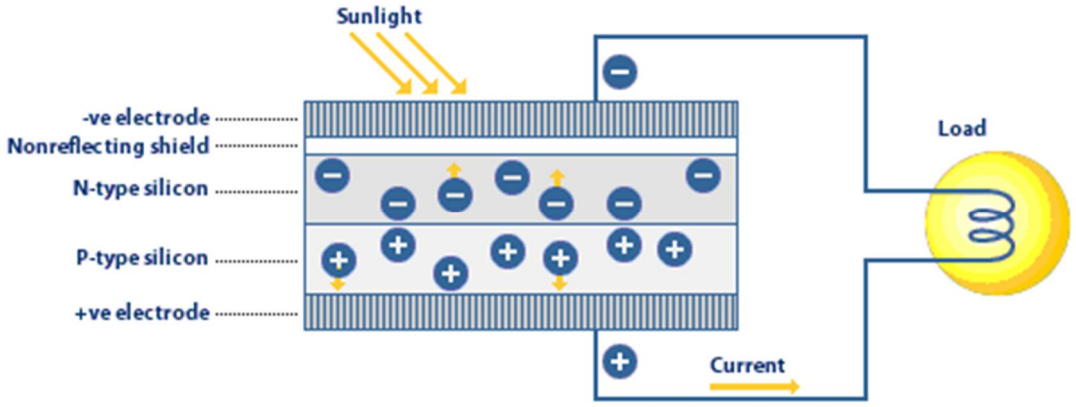

Figure 3: Structure of a PV cell [34]

When an external load are connected to the 2 layers, electrons that flow through the circuit create electricity as shown in Figure 3. Each individual solar energy cell produces only a few watts. In order to increase power output, cells are integrated in a weather-tight package called a solar module. These modules are then connected in series and/or parallel with one another, into a solar array, to create the desired voltage and amperage output required by the given system.

Thanks to the wide availability of silicon, which is the semi-conductor material that PV cells are primarily made of, and the natural abundance the sunlight, solar cells are very environmental friendly. They burn no fuel and have absolutely no waste which makes them pollution free, clean, and silent [5].

1.3 Effect of Irradiance and Temperature of PV Cell

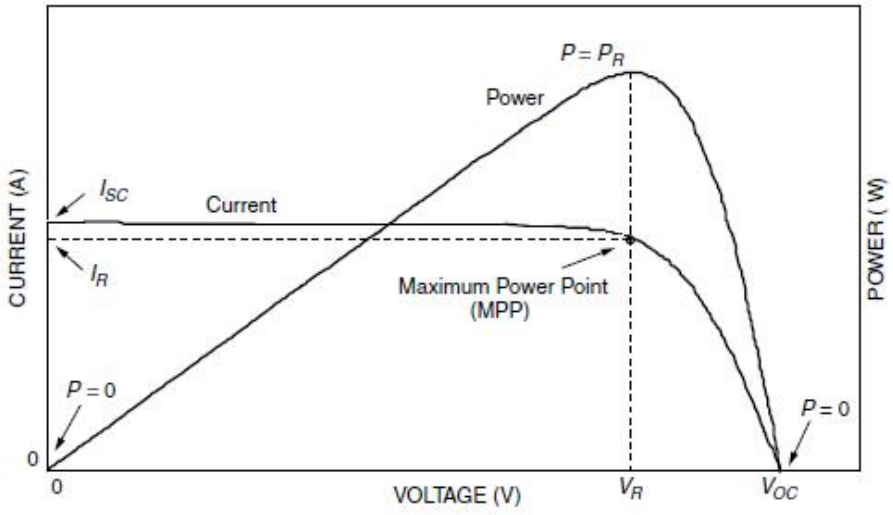

Figure 4: I-V curve and power output for a PV module. At MPP, the module delivers the most power. [35]

Figure 4 and 5 illustrates the current-voltage characteristics I–V and power-voltage P–V of the PV cell for different levels of irradiance. The short-circuited current I_{sc} increases quasi-linearly with irradiance and the voltage V_{oc} increases slightly. In addition, the maximum power P_{MPP} increases as the irradiance increases, therefore, the higher irradiance the higher the efficiency.

The standard conditions are generally chosen with an irradiance of 1000 W/m^2 or full-sun at cell temperature of 25 degree Celsius. In fact, the irradiance on PV without light concentration is lower, and, thus, the overall power is lower than its rated value.

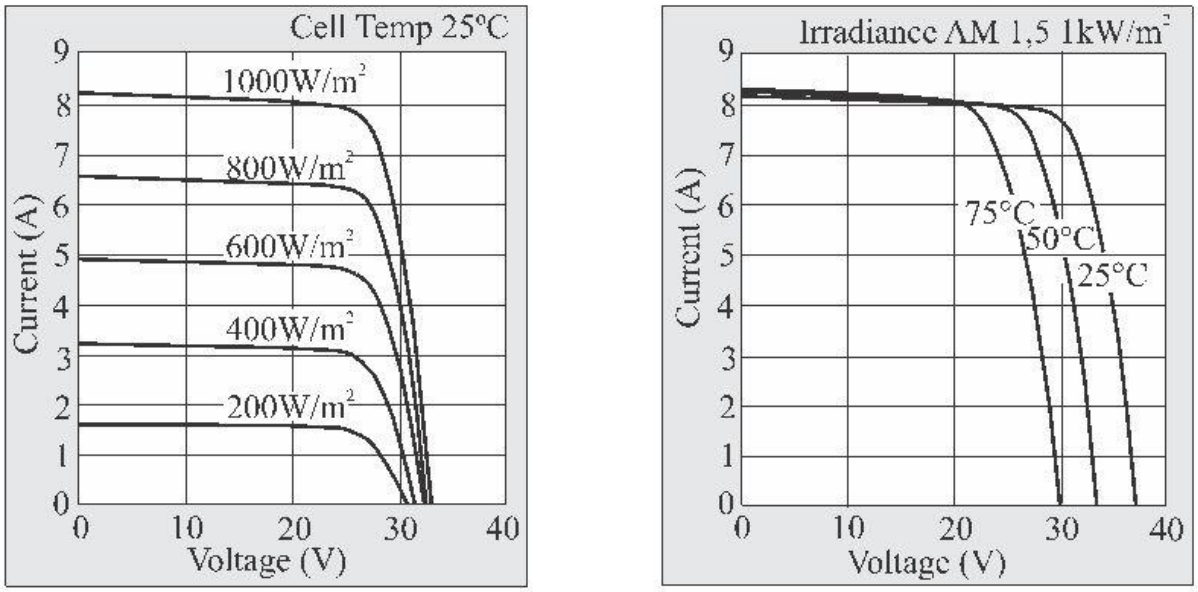

Fig 5: Effect of Cell Temperature and Irradiance on PV cell [35]

When the cell temperature T increases, the short circuit current I_{sc} increase slightly due to better absorption of light (because the energy gap decreases with temperature) but the open-circuit V_{oc} voltage greatly decreases with temperature. Hence, the maximum power P_{MPP} also strongly decreases with temperature. Under hot ambient temperature, the cell temperature is often higher and thus the efficiency lower. Solar cell reach its highest efficiency during winter and clear sky condition.

1.4 Common Thermal-Related Applications of PV

The PV system, due to its potential, has become larger and more diverse with so many applications ranging from consumer electronics to grid-connected-PV to PV in space. Among those, there are many cases where temperature of PV cells is an essential information for the system to operate efficiently and correctly. In a large scale PV system, managing temperature of PV panels could be helpful to quickly identify fault in panels. For PV in extreme condition like PV in desert as shown in Fig 6(a), the high ambient temperature can cause low efficiency due to PV characteristic shifting. Having the temperature model to update the PV cells temperature can help to increase overall efficiency. PV concentrators like the one in Fig 6(b) is also a field where cell temperature is important for managing operating threshold and possible fault detection. Furthermore, PV in space, which also use high power PV concentrator like in Fig 6(c), is sensitive to the sudden change of ambient temperature and surrounding system.

(a) PV in desert [36]

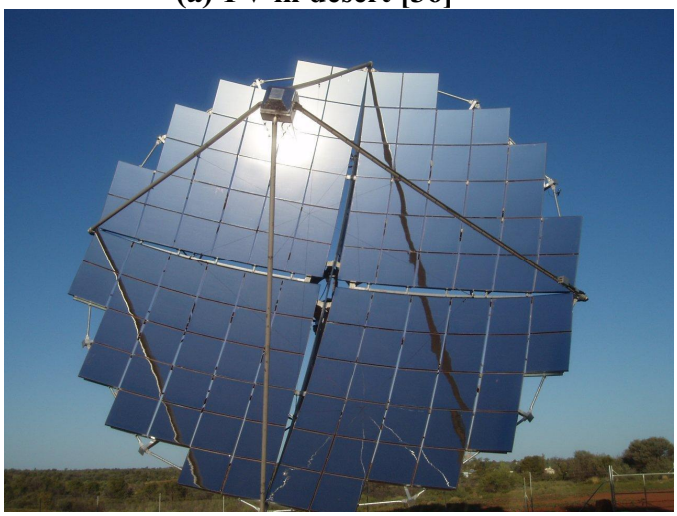

(b) PV concentrators [37]

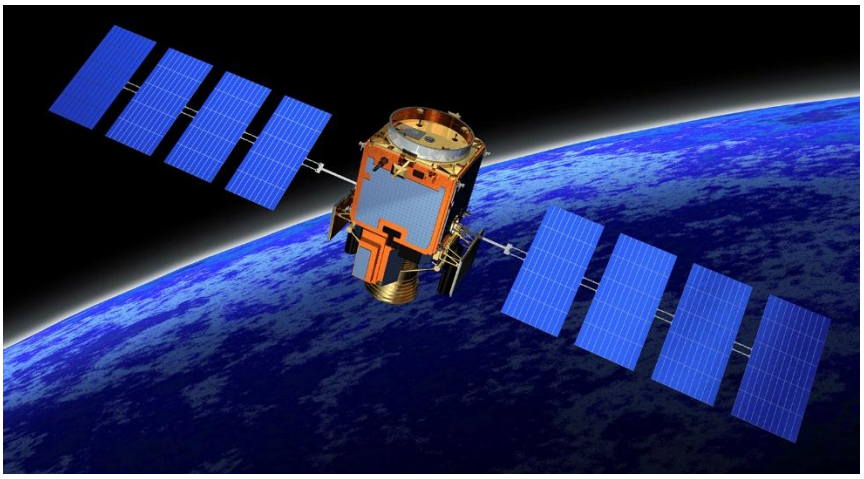

(c) PV in space

Figure 6: Common thermal-related applications of PV [38]

CHAPTER 2

ELECTRIC-THERMAL PV MODEL

2.1 Electric Model

A PV cell incorporates parasitic resistances, capacitances, and inductances that can be modelled using circuit components, with a current source representing photocurrent. The parameters involved in the single-diode model consist of a photocurrent source I_{ph}, forward-biased conducting diode D_f, shunt resistance R_{sh} and series resistance R_s. This model includes a series inductance Ls and variable parallel capacitance C_p as dynamic components, as well as a reverse-bias conducting diode D_r and breakdown voltage offset V_{bd} [14], [25], [26] as reverse-bias components, as shown in Fig. 7.

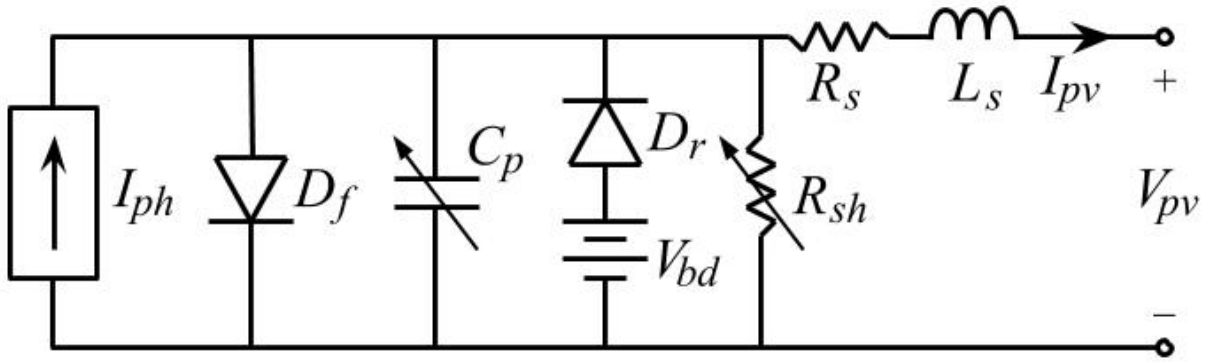

Figure 7: Equivalent circuit for a dynamic PV cell [14]

The governing equations of this electrical model are based on the equivalent circuit shown in Fig. 7. After calculating all parallel components relative to the PV model input (irradiance G, cell temperature T, PV current I_{pv}), the voltage over the forward diode V_d is solved for using a nonlinear solving technique, such as Newton-Rhapson or Halley's Method [7]. Then, the PV output voltage is calculated based on V_d and I_{pv} using Kirchhoff's voltage law. The following equations describe all the relations in the electrical model. Derivation and detailed explanation for the following electrical model equations can be found in [14]. All model variables and units are listed in Table I. Note that the model inputs (G, T, M, and I_{pv}) can be dynamically changed during simulation to affect the model output (V_{pv}), but parameters are fixed values.

Model Input	
G	irradiance $[W/m^2]$
T	temperature $[K]$
M	air mass coefficient
I_{pv}	PV current $[A]$
Model Output	
V_{pv}	PV voltage $[V]$
Parameters	
k	Boltzmann constant $[J/K]$
q	electron charge $[C]$
G_n	nominal irradiance $[W/m^2]$
T_n	nominal temperature $[K]$
M_n	nominal air mass coefficient
I_{scn}	nominal short circuit current $[A]$
V_{ocn}	nominal open circuit voltage $[V]$
I_{mpp}	maximum power point current $[A]$
V_{mpp}	maximum power point voltage $[V]$
K_i	current temperature coefficient $[A/K]$
K_v	voltage temperature coefficient $[V/K]$
N_s	number of cells in series
R_s	series resistance $[\Omega]$
R_{shn}	nominal shunt resistance $[\Omega]$
L_s	series inductance $[H]$
a	diode ideality factor
V_{bd}	breakdown voltage $[V]$ (negative value)
I_{sr}	reverse saturation current $[A]$
K_r	reverse breakdown scalar coefficient
C_{j0}	zero-bias junction capacitance $[F]$
ϕ_0	zero-bias junction potential $[V]$
τ	mean carrier lifetime $[s]$
τ_{bd}	breakdown mean carrier lifetime $[s]$

TABLE I: PV MODEL VARIABLES

2.1.1 Photocurrent:

Photocurrent I_{ph} is the flow of electron excited by incoming irradiation from the sun G, air mass modifier M, and difference between the PV temperature T and nominal temperature T_n, which is defined as follows

$$I_{ph}(G,T) = \left[I_{scn}\left(\frac{R_s + R_{sh}}{R_{sh}}\right) + K_i(T - T_n)\right]\frac{G}{G_n}\frac{M}{M_n} \qquad (1)$$

where I_{scn} is the nominal short-circuit current, Ki is the current temperature coefficient, G_n is the nominal irradiance, and M_n is the nominal air mass. As can be seen in equation (1), the photocurrent is a dynamic variable which is affected by the input to the system which is temperature, irradiance and air mass ratio.

Because the spectral absorption of gas in the atmosphere could change slightly with different air mass, which in turn alter the spectral distribution of incoming irradiance on PV panel, hence affecting the generated photocurrent. This systematic influence is included in equation (1) to better describe the change in PV generated current due to environmental change.

2.1.2 Diodes:

The thermal voltage V_t is an important factor in both the forward and reverse diodes, defined as

$$V_t(T) = \frac{kT}{q} N_s \qquad (2)$$

where k is the Boltzmann constant, q is the electron charge, and Ns is the number of cells in series. The forward diode D_f conducts current I_{df} when the PV is forward biased, and the governing equation for its current is

$$I_{df}(T, V_d) = I_s(T)\left[\exp\left(\frac{V_d}{aV_t(T)}\right) - 1\right] \qquad (3)$$

where a is ideality factor of diode, which measures how closely the diode follows the ideal diode equation; its value usually ranges from 1 to 2. The diode saturation current I_s is

$$I_s(T) = \frac{I_{scn} + K_i(T - T_n)}{\exp\left(\frac{V_{ocn} + K_v(T - T_n)}{aV_t(T)}\right) - 1} \qquad (4)$$

where V_{ocn} is the nominal open circuit voltage, and K_v is the voltage temperature coefficient. The reverse diode D_r conducts when PV is reverse biased, and the governing equation for its current I_{dr} is

$$I_{dr}(T, V_d) = I_{sr} \exp\left(\frac{K_r V_{bd}}{aV_t(T)}\right)\left[exp\left(\frac{-K_r V_d}{aV_t(T)}\right) - 1\right] \qquad (5)$$

where I_{sr} is the reverse saturation current and K_r is the reverse breakdown scalar coefficient.

2.1.3 Parallel Capacitor:

PV parallel capacitance C_p is a lumped value which consists of three different sources: junction capacitance C_j, diffusion capacitance C_d, and breakdown capacitance C_{bd}. The overall parallel capacitance C_p is

$$C_p(T,V_d) = C_j(V_d) + C_d(T,V_d) + C_{bd}(V_d)$$
$$= \frac{C_{jo}}{N_s\sqrt{1-\frac{V_d}{\phi_0}}} + \frac{\tau I_{df}(T,V_d)}{aV_t(T)} + \frac{\tau_{bd} I_{dr}(T,V_d)}{aV_t(T)} \quad (6)$$

where C_{j0} is zero-bias junction capacitance, ϕ_0 is zero-bias junction potential, τ is mean carrier lifetime, and τ_{bd} is breakdown mean carrier lifetime. Parallel capacitance current I_{Cp} is described as

$$I_{Cp}(V_d) = C_p(T,V_d)\frac{dV_d}{dt} \quad (7)$$

2.1.4 Shunt Resistance:

The shunt resistance R_{sh} is inversely proportional to the incoming illumination since the effective shunt resistance increases as illumination decreases, and it is defined as

$$R_{sh}(G) = R_{shn}\frac{G_n}{G} \quad (8)$$

where R_{shn} is the nominal shunt resistance. The effective shunt resistance increases when the incoming irradiance decreases, therefore R_{shn} is inversely proportional to G. Shunt resistor current I_{Rsh} is

$$I_{Rsh}(G,V_d) = \frac{V_d}{R_{sh}(G)} \quad (9)$$

2.1.5 Diode Voltage:

After obtaining these currents, Kirchhoff's Current Law is applied, which leads to the nonlinear equation

$$0 = I_{ph}(G,T) - I_{df}(T,V_d) - I_{Cp}(V_d) + I_{dr}(T,V_d) - I_{Rsh}(G,V_d) - I_{pv} \quad (10)$$

With given inputs (illumination G, PV temperature T and PV current I_{pv}), this equation is solved for V_d by employing a nonlinear solving technique.

2.1.6 PV Voltage:

Output PV voltage V_{pv} can then be calculated according to

$$V_{pv}(V_d, I_{pv}) = V_d - I_{pv}R_s - L_s\frac{dI_{pv}}{dt} \qquad (11)$$

Equation (1) to (11) fully define the PV electrical model. Compared to the model given in [14], equations (1) and (9) have been updated.

2.1.7 Nonlinear solving techniques:

In equation (10), the output of the PV cells cannot be solved for explicitly using common elementary functions but requires nonlinear solving techniques. In this work, the Newton-Raphson method is adopted which is a widely-used nonlinear solver for obtaining roots of implicit transcendental equations. This method is popular in the field of iterative computational applications because of its simplicity and fast convergence.

At first, an initial guess of V_d is calculated based on nominal maximum power voltage. Then, by using this initial value of V_d, parameters which is depend on V_d will be calculated such as forward and reverse diode current, shunt resistance current and parallel capacitance current. After that, the right side of equation (10) will be calculated and the results will go through a loop to keep it within an acceptable tolerance value (0.0001 in this work). In this checking loop, after every iteration, the value of V_d is updated until the left side of equation (10) is as close as possible to 0 (within a tolerance of 0.0001). Then, the output voltage and power of PV cells is calculated based on the new V_d value.

2.2 Thermal Model

For the thermal model, the temperature and heat distribution of the PV cell also need to be determined accurately. The thermal model is composed of five layers, according to the test setup: top glass, top air gap, crystalline PV cell, bottom air gap and bottom glass, as shown in Fig. 8.

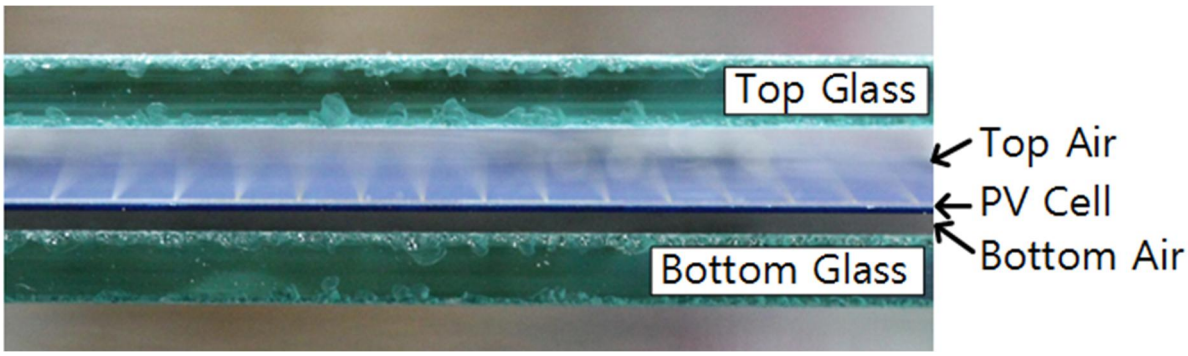

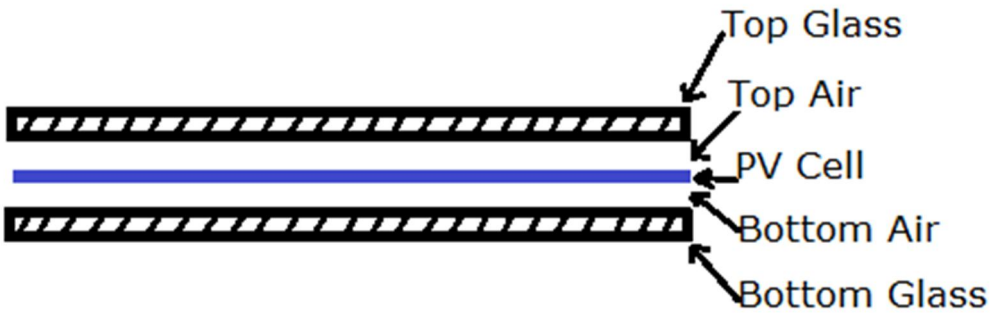

Figure 8: Cross section of the PV cell test setup

The model temperature is determined by calculating the thermal energy exchange of each layer with its environment and surrounding layers through the main heat transfer paths of conduction, convection, and radiation as shown in Fig. 9 [27], [28], [29], [30].

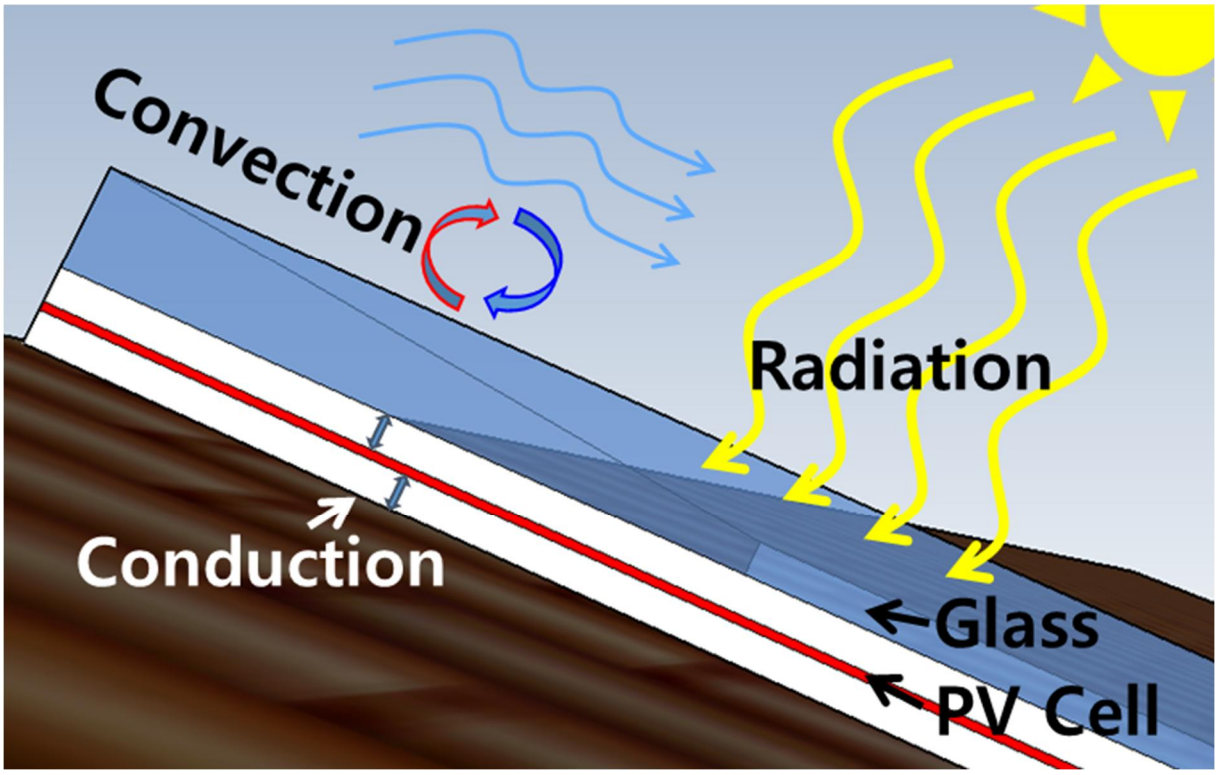

Figure 9: Heat transfer paths throughout the PV panel

The general equation for the temperature change rate for a layer is described as

$$C_{lx}\frac{dT}{dt} = Q_{lw} + Q_{sw} + Q_{convx} + Q_{lx-y} - P_{out} \qquad (12)$$

where C_{lx} is the total heat capacity of layer x, Q_{lw} is heat flow generated by long wave radiation, Q_{sw} is heat flow generated by short wave radiation, Q_{convx} is heat flow due to convection for layer x, Q_{lx-y} is

conduction heat flow to layer x from an adjacent layer y, and Pout is the electrical energy loss generated in the layer. The general equation for convection heat transfer for layer x can be described as

$$Q_{convx} = \left(h_{c,for} + h_{c,free}\right)A_{lx}(T_{amb} - T_{lx}) \quad (13)$$

where A_{lx} is the area of layer x, $h_{c,for}$ = 1 $Wm^{-2}K^{-1}$ is the forced convection coefficient, $h_{c,free}$ = $0{:}655(T_{lx} - T_{amb})^{\frac{1}{3}}$ $Wm^{-2}K^{-1}$ is the free convection coefficient, T_{amb} is ambient temperature, and T_{lx} is temperature of layer x [31]. The general equation for heat flow to layer x from adjacent layer y is described as

$$Q_{lx-y} = U_{ly}A_{ly}\left(T_{ly} - T_{lx}\right) \quad (14)$$

where U_{ly} is heat transfer coefficient from layer y. Total heat capacity of layer x is determined by

$$C_{lx} = C_{m-lx}\rho_{lx}d_{lx}A_{lx} \quad (15)$$

where C_{m-lx} is specific heat capacity, ρ_{lx} is density, and dlx is thickness of the layer. Each layer is defined based on (12), according to the heat transfer path that the layer experiences.

2.2.1 Layer 1: Top Glass:

In the top glass layer, convection heat transfer between the glass surface and surrounding air in the environment and the conduction heat flow from layer 2 affect the overall thermal exchange in the layer. The heat transfer equation for the top glass is

$$C_{l1}\frac{dT_{l1}}{dt} = Q_{conv1} + Q_{l1-2} \quad (16)$$

where C_{l1} is the total heat capacity of layer 1 and C_{l1-2} is heat flow from the top air gap.

2.2.2 Layer 2: Top Air Gap:

The air gap is a medium for heat exchange between the two adjacent layers. Hence, the heat transfer equation for this air layer is determined by

$$C_{l2}\frac{dT_{l2}}{dt} = Q_{l2-1} + Q_{l2-3} \quad (17)$$

where Q_{l2-1} is heat flow from the top glass and Q_{l2-3} is heat flow from the crystalline PV cell.

2.2.3 Layer 3: Crystalline PV Cell:

For the crystalline PV cell, short wave and long wave radiation heat transfer, heat flow from adjacent layers, and heat generated by electrical energy contribute to the heat transfer equation, according to

$$C_{l3}\frac{dT_{l3}}{dt} = Q_{sw} + Q_{lw} + Q_{l3-2} + Q_{l3-4} + Q_{ele} \quad (18)$$

Where Q_{l3-2} is heat flow from layer 2, Q_{l3-4} is heat flow from layer 4, and Q_{ele} is heat generated from electric loss. Heat transfer from short wave radiation is

$$Q_{sw} = \alpha_{ab} G A_{l3} \quad (19)$$

where α_{ab} = 0.77 is the absorbability of cell surface, G is the total incident irradiance, A_{l3} is the area of layer 3. Heat transfer from long wave radiation is

$$Q_{lw} = \sigma A_{l3}\left(\frac{1+cosB}{2}e_s T_s^4 + \frac{1-cosB}{2}e_g T_g^4 - e_p T^4\right) \quad (20)$$

where σ is Stefan-Boltzmann constant, B is the tilted surface angle from the horizontal, e_s = 0.95 is the emissivity of the sky, T_s = Tamb - 20K is the effective sky temperature, e_g = 0.95 is the emissivity of the ground surface, T_g is the ground temperature, and e_p = 0.9 is the emissivity of the PV panel. Finally, the heat generated in the PV cell is defined as

$$Q_{ele} = R_s I_{pv}^2 + \frac{\left(V_{pv} + R_s I_{pv}\right)^2}{R_{sh}} - V_{pv} I_{pv} \quad (21)$$

where I_{pv} and V_{pv} are values from the electrical PV model [32] [33].

2.2.4 Layer 4: Bottom Air Gap:

The bottom air gap is also a medium for heat exchange between the two adjacent layers. Hence, the heat transfer equation for this air layer is determined by

$$C_{l4} = \frac{dT_{l4}}{dt} = Q_{l4-3} + Q_{l4-5} \quad (22)$$

where Q_{l4-3} is heat flow from the crystalline PV cell and Q_{l4-5} is heat flow from the bottom glass.

2.2.5 Layer 5: Bottom Glass:

In the bottom glass layer, the convection heat transfer between the glass surface and surrounding air in the environment and heat flow from layer 4 affect the overall thermal exchange in the layer. The heat transfer equation for the bottom glass is

$$C_{l5}\frac{dT_{l5}}{dt} = Q_{conv5} + Q_{l5-4} \quad (23)$$

where Q_{l5-4} is heat flow from the bottom air gap. After obtaining total heat capacity and relevant heat flow for each layer, the temperature rate of change $\frac{dT_{k+1}}{dt}$ over the simulation time step interval h is calculated. Then, it is added to the layer temperature of the previous time step T_k to determine the current temperature T_{k+1}, as follows

$$T_{k+1} = T_k + \frac{dT_{k+1}}{dt}h \quad (24)$$

2.3 Electric and Thermal Model Interaction

The electric and thermal PV models were combined into one model and built in MATLAB/Simulink and RT-LAB software, which is used for real-time PHILS operation. Fig. 10(a) shows the combined Simulink model, Fig. 10(b) shows the electrical block, and Fig. 10(c) shows the thermal block. There are three main subsystems: electrical model, thermal model and the console. The console subsystem is where the user can manage all the input parameters to the system, such as PV current, illumination, air mass modifier, state of the bypass diode (with or without a parallel bypass diode), ambient temperature, ground temperature, and number of PV in series. The electrical subsystem contains all the governing equations for the electrical model. After receiving all the necessary inputs from the console block, i.e., PV current, illumination, air mass modifier, and bypass diode state, this subsystem will calculate the output voltage and power of the PV system. Note that other PV models, such as the double-diode model [34], could be implemented in the electrical model block as long as the same output signals are produced. The electrical model output becomes input for the thermal subsystem, which determines the temperature of all five layers in the PV system.

The PV cell temperature is fed back into the electrical model to accurately adjust the PV electrical model. All of the outputs of the system (PV voltage and power, each layer temperature, and processing time of the electrical and thermal block) can be observed through the console block in real-time simulation. The electrical and thermal blocks model operate at the same time using parallel computation, with two cores for fast processing time: one core for the electrical model and one core for the thermal model [7], [8].

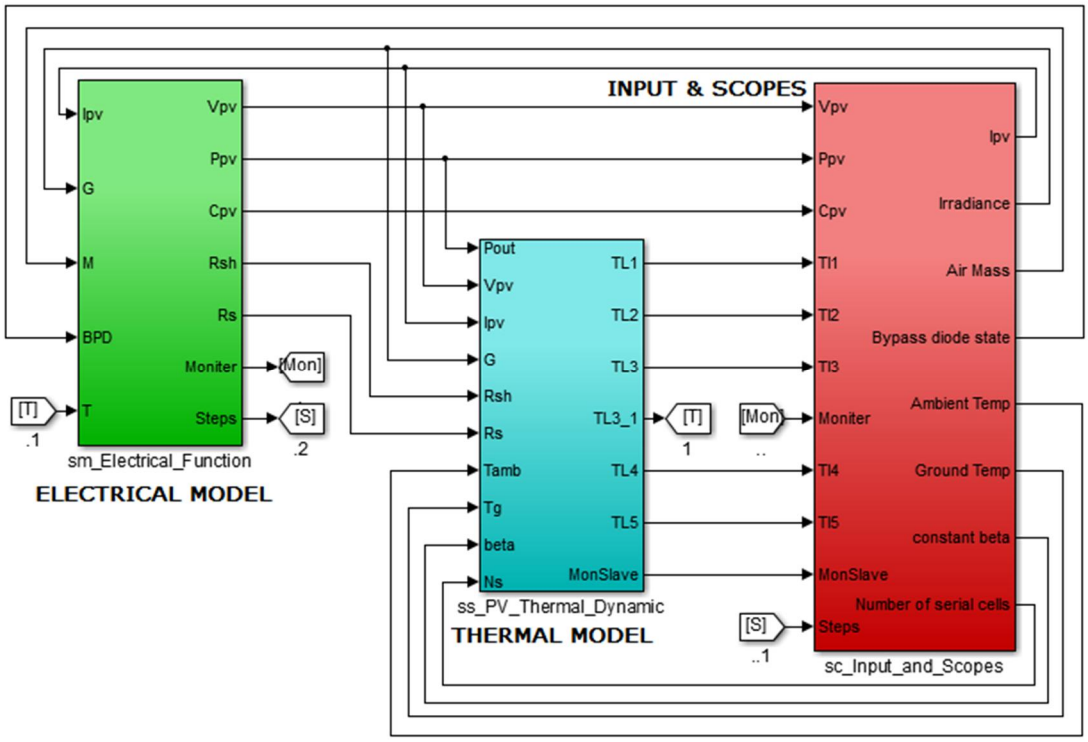

(a)

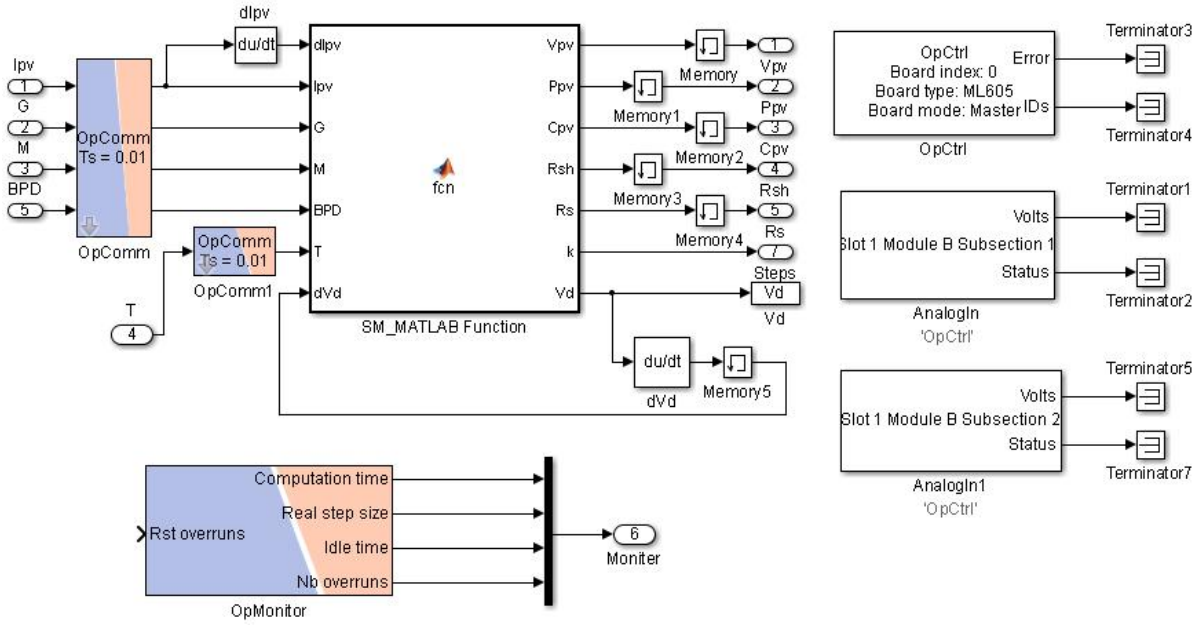

(b)

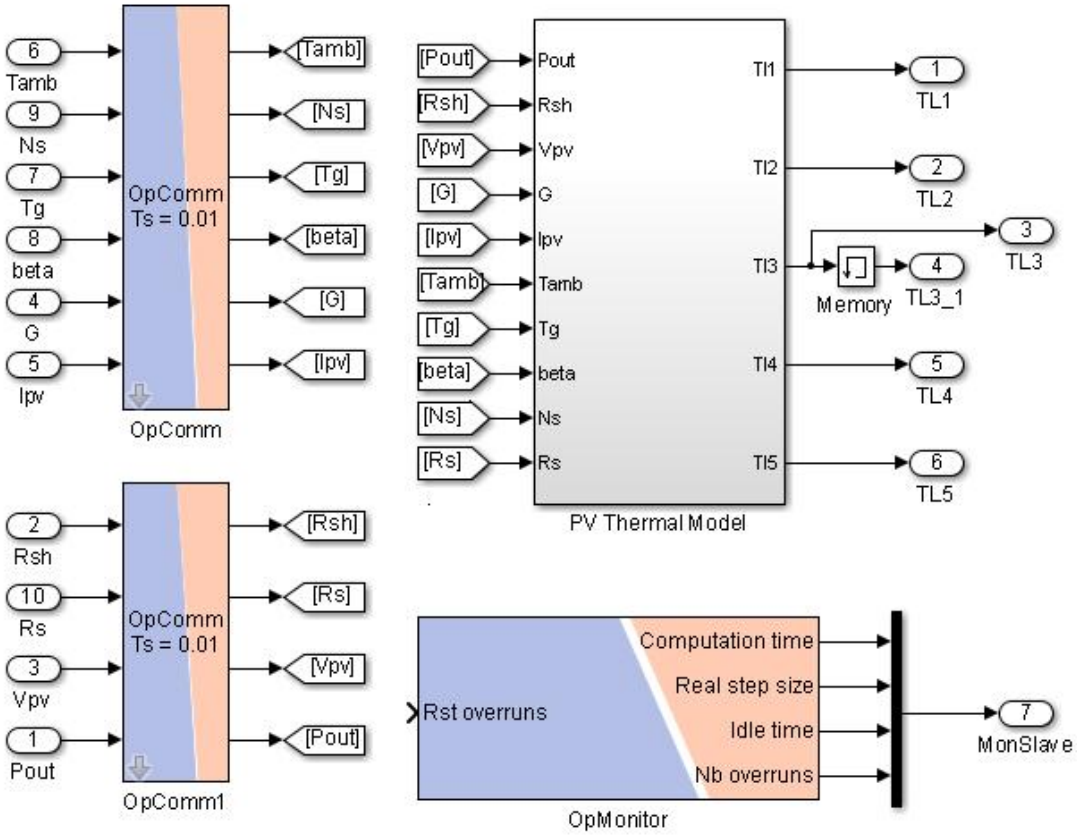

(c)

Figure 10: Simulink models of the (a) electric-thermal PV model, (b) electrical model block, and (c) thermal model block

CHAPTER 3

EXPERIMENTAL SETUP

In this section, the accuracy and performance of the electric-thermal PV model is verified versus experimental results. There are two experimental setups: 1) setup to measure characteristics of a real PV cell and 2) PHILS setup to test the model's capability to interface with power hardware in real time. The model is validated using static tests to validate the electrical portion of the model and dynamic PHILS tests to validate the full model.

3.1 PV cell experimental Setup

To verify model accuracy, the electrical and thermal characteristics of a 1.3-W crystalline PV cell was tested using a Keithley 2430 SourceMeter, which can function as either a dc power source or load. For both static and dynamic tests, the PV electrical characteristics are controlled and measured using the sourcemeter. To measure the PV thermal characteristics, a custom testing device was constructed that holds a single PV cell between two planes of glass. Two thermals couples are used; one is attached to the back of the cell to measure the cell temperature and one is attached to the back of the bottom glass to measure the bottom glass temperature. Two Kikusui DME1600 Digital Multimeters in thermal-couple mode were used to measure cell and glass temperatures. The PV testing device and experimental setup is shown in Fig. 11.

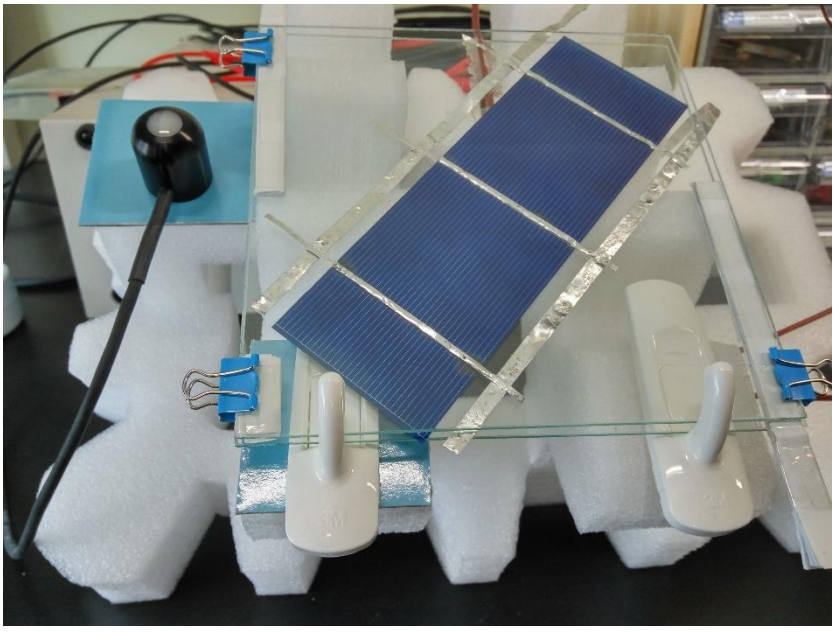

(a) Closer look at the PV setup

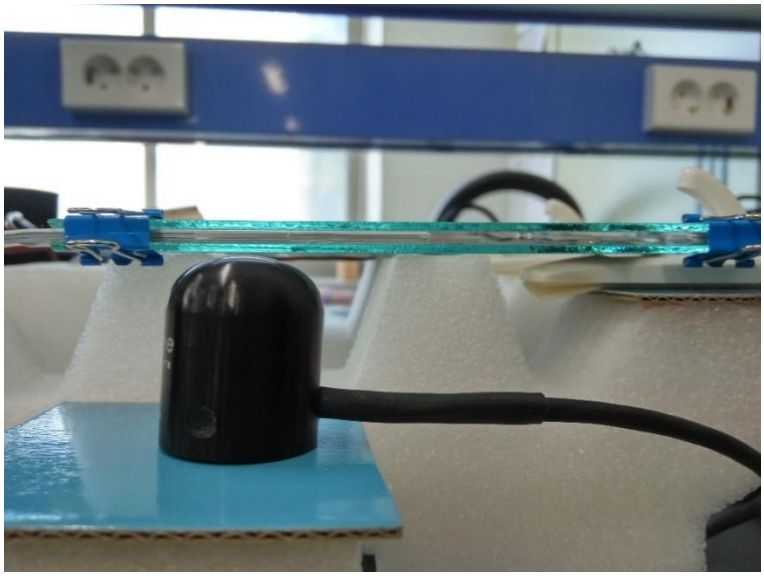

(b) Pyranometer is used to record incoming irradiance

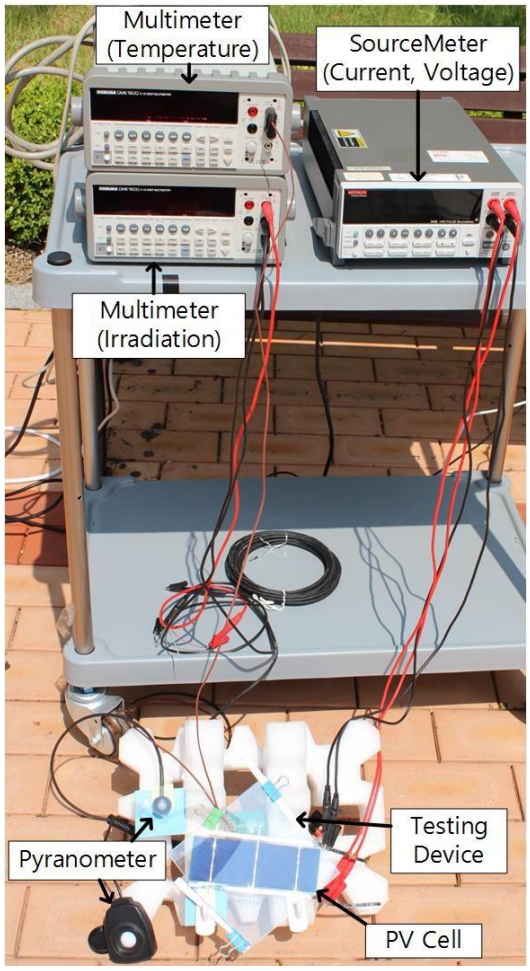

(c) Out door experimental setup

Figure 11: PV Cell Experimental Setup

3.2 PHILS Setup

The PHILS setup is shown in Fig. 12. The PV model is implemented using MATLAB/Simulink software and compiled in the RT-LAB computer program. Then, it is downloaded into the OPAL-RT OP5600 simulator. The PV model inputs are irradiance and PV current. The input irradiance is based on irradiance data recorded during the tests on the PV cell. The PV current is measured from a Kikusui PAT 80-100T programmable DC power supply and fed back into the model. Based on these inputs, the real-time simulator calculates the output PV voltage and the layer temperatures. The programmable DC power supply receives output voltage commands from the simulator and adjusts its output voltage accordingly to emulate the PV cell. The power supply is connected to the sourcemeter, which is used instead of power converter hardware. A Python program commands the sourcemeter to create various load changes in the output current to examine the performance of the PHILS-emulated PV cell.

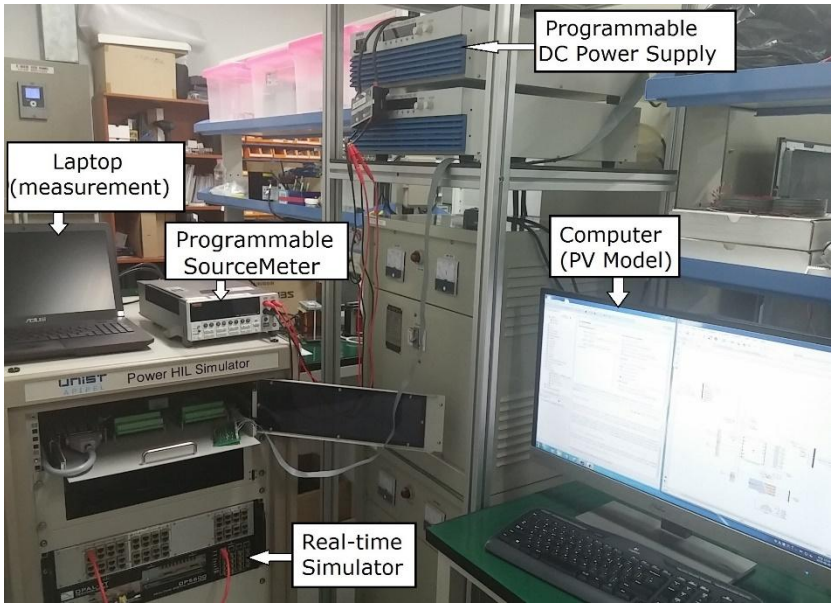

Figure 12: PHILS Setup

CHAPTER 4

ELECTRIC-THERMAL PV MODEL VALIDATION

4.1 Parameter values

In order to model the 1.3-W crystalline PV cell tested in experiment, model parameters must be extracted. The nominal maximum power point voltage and current was taken from the datasheet as characteristic inputs of the electrical model. The short circuit current, open circuit voltage and breakdown voltage were obtained from experimental testing. The air mass coefficient is chosen to be 1.5 due to the zenith angle of the PV setup and the location of the author is in temperate latitude country. For reference, the air mass coefficient is 0 for PV in space, 1 for 0 degree zenith angle or equatorial or tropical region, 1.5 for zenith angle of about 48.2 degree or temperate latitude region and 2 or 3 for high latitude region such as northern Europe. Other intrinsic parameters, such as series and shunt resistance, diode ideality factor, reverse saturation current, and reverse breakdown shaping factor, are obtained from a separate parameter-fitting procedure, detailed in [14]. All of the input parameters for the electrical PV model are shown in Table II.

The area and thickness of the five testing device layers were measured using a digital caliper. Other parameters used to calculate the total heat capacity and heat transfer coefficient of each layer, such as density and specific heat capacity, were found in [7], [17] and the datasheets. Parameters of all five layers are given in Table III.

TALBLE II: PV MODEL INPUT PARAMETERS

PV Model Input	
V_{mpn}	0.4461 $[V]$
I_{mpn}	1.957 $[A]$
I_{scn}	2.11 $[A]$
V_{ocn}	0.5566 $[V]$
N_s	1 $[cell]$
V_{bd}	-15 $[V]$
R_s	0.015 $[\Omega]$
R_{sh}	210 $[\Omega]$
a	1
I_{sr}	0.1053 $[A]$
K_r	0.0278
M_n	1.5

TABLE III: THERMAL PROPERTIES FOR THE FIVE PV SYSTEM LAYERS

Layer	A_{lx} $[m^2]$	U_{lx} $[W/m^2K]$	C_m $[J/K]$
Top Glass	0.0225	9.3517	69.525
Top Air Gap	0.0225	9.5976	0.0299
Crystalline PV Cell	0.00806	9.5976	2.924
Bottom Air Gap	0.0225	9.5976	0.0299
Bottom Glass	0.0225	9.3517	69.525

4.2 Static Condition Verification

4.2.1 Multiple I-V Curve with Different Irradiance (Forward and Reverse-bias Region):

In this section, the electrical and thermal aspects of the model are validated in static conditions using off-line simulation. The purpose of this static condition verification is to ensure that the model is accurate enough to be used further in real-time simulation. Four current-voltage (I-V) curves at four different irradiance levels are recorded using the experimental test setup by performing voltage sweeps from the cell's open circuit voltage to -13 V. By choosing this voltage range, the electrical aspect of the model can be examined in both forward- and reverse-bias regions.

Experiments were taken under irradiance levels of 355, 910, 980, and 1060 W/m2 with ambient temperature of about 301 K. The model was simulated under the same conditions and the results are shown in Fig. 13. Fig. 13(a) shows the similarity between the experimental and simulated electrical characteristic data, which exhibits error within 1.18%. The measured and simulated cell temperature for the four tests are shown in Fig. 13(b). For both experimental and simulation temperature results, the cell temperature begins to increase at the end of the sweep because the cell becomes reverse biased, acting acts as a load instead of a source and generating heat. The thermal aspects of the model show very accurate results in the forward-bias region but have some deviation in the reverse-bias region near the breakdown region, with the highest difference of 1.5 K. Since the sweep is conducted relatively quickly, the measured cell temperature experiences a sudden increase, but the model's temperature calculation lags behind by 2 to 3 seconds before increasing. Overall, the cell temperature results are relatively well matched, with error within 1.48%. All error values are calculated using the mean relative error (MRE) criterion:

$$MRE(\%) = 100 * \frac{1}{N} \sum_{k=1}^{n} \left| \frac{exp - sim}{exp} \right| \qquad (24)$$

where *exp* and *sim* stand for experiment and simulation data, and N is the number of samples, respectively.

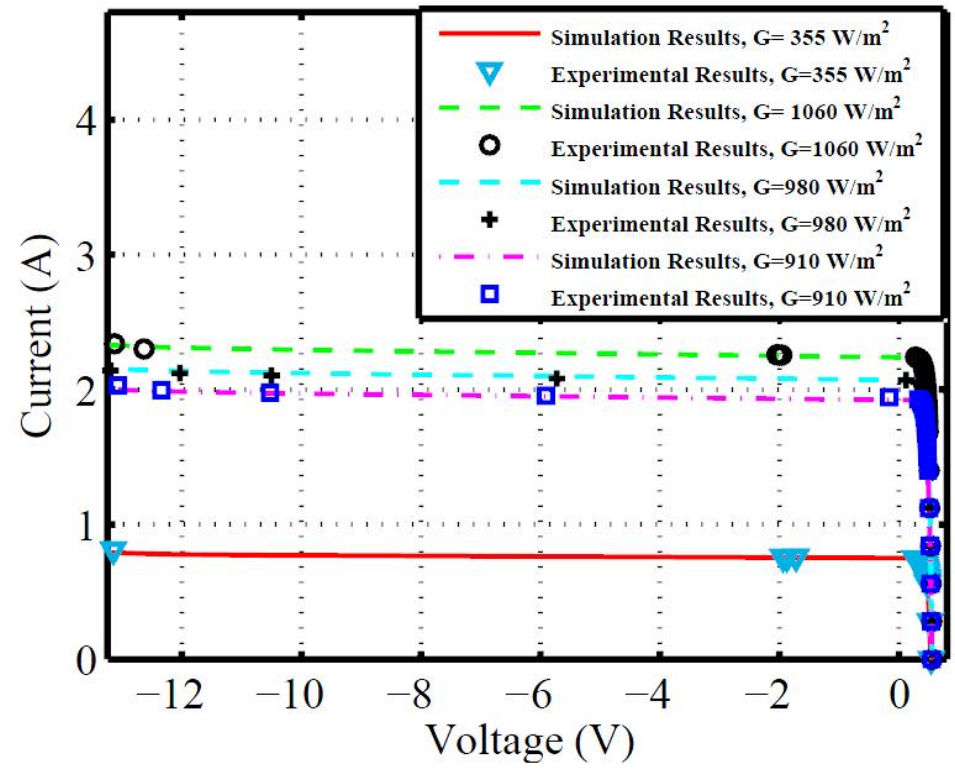

(a)

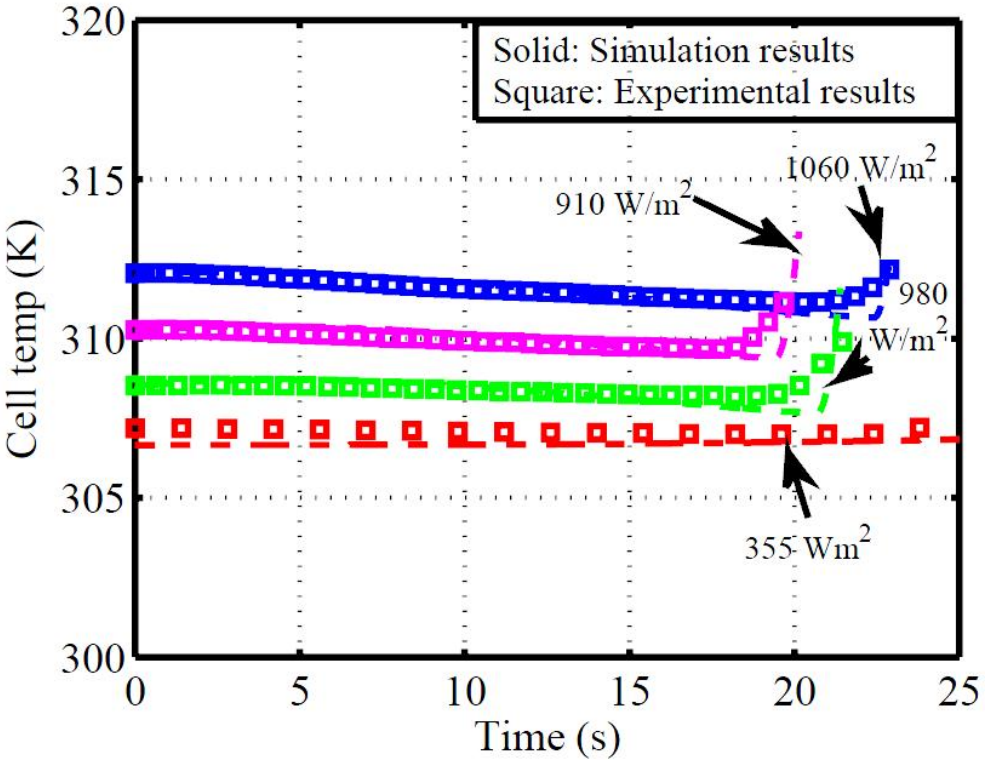

(b)

Figure 13: Static condition testing results of the electric-thermal PV model at multiple irradiance levels: (a) I-V curves and (b) PV cell temperature.

4.2.2 Reverse-bias Characteristic Validation:

In order to validate the performance of the PV model in the reverse-bias region and the effect of PV cell's temperature on its electrical characteristics, another test is conducted. First, a current sweep is performed from the cell's open circuit voltage to -17.8 V in dark conditions (0 W/m^2) with ambient temperature of about 293 K, and then the last operating point is held for 60 sec to observe change in the cell's electrical characteristics. The Simulink PV model was simulated under the same conditions and was compared with the experimental results, as shown in Fig. 14(a). When the cell's operating point moves into the reverse-bias region, the cell acts as load instead of a power source. Hence, it generates heat, which leads to a sudden increase in the cell's temperature. As the temperature increases, the cell's operating voltage decreases in the reverse-bias region, as shown in Fig. 14(b). The simulation results are well matched with the measured data, yielding an error of 2.85%.

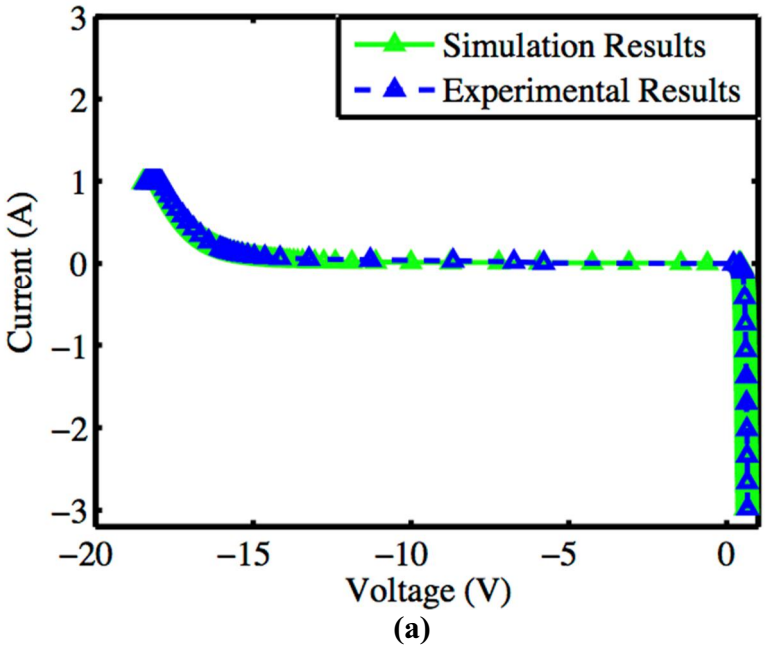

(a)

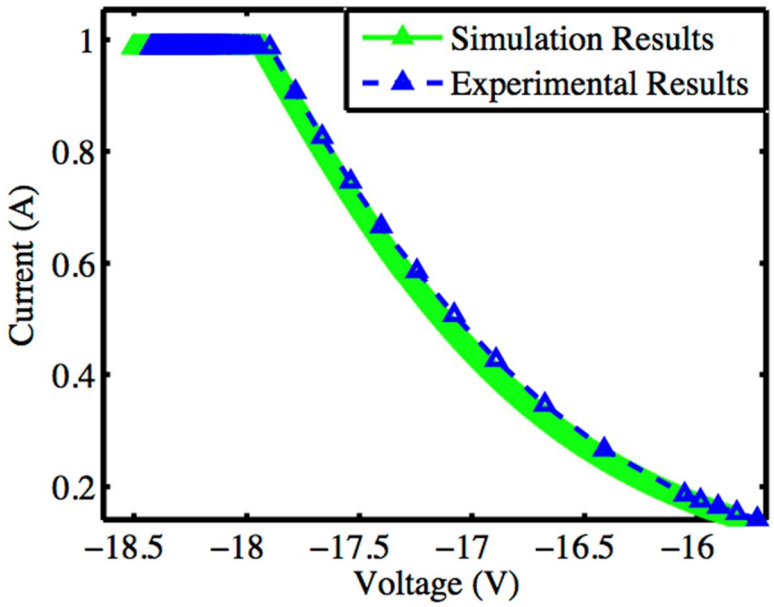

(b)

Figure 14: I-V curve comparison between simulation and experimental result under dark test condition (a) full I-V curve and (b) reverse-bias region where operating point is hold at constant for 60 sec

4.2.3 Fixed PV Voltage Operation

The thermal model in Simulink is examined under an insolation of 1060 W/m^2 and the operating point is fixed at a constant voltage level of 0.4 V with ambient temperature of 304 K. The simulation is run under the same conditions for 480 sec, and the cell's temperature results are compared in Fig. 15. As shown, the average simulation cell temperature is 325.9 K, which is close to results from the experiment 327.8 K. The settling time of the simulation is about 70 s, which is relatively fast compare to the actual temperature settling rate. Fig. 15(b) shows that the simulation and experimental data are well matched, with 2.51% error.

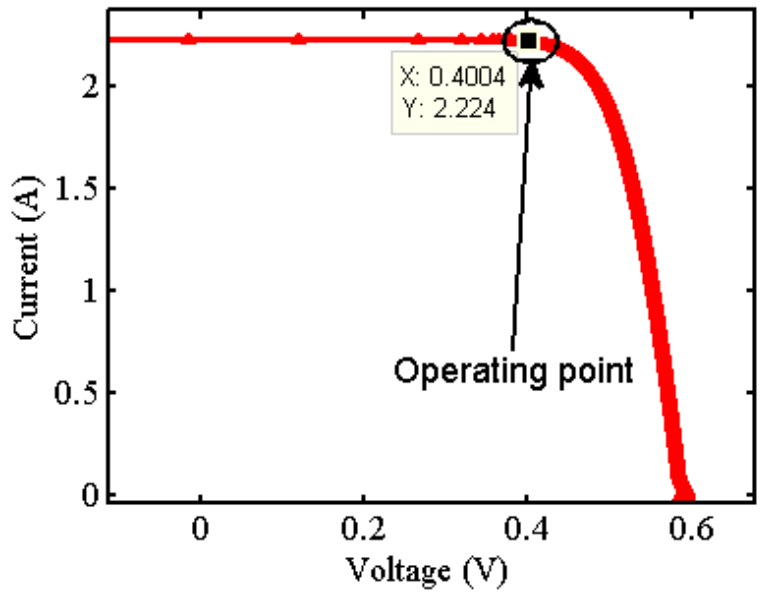

(a)

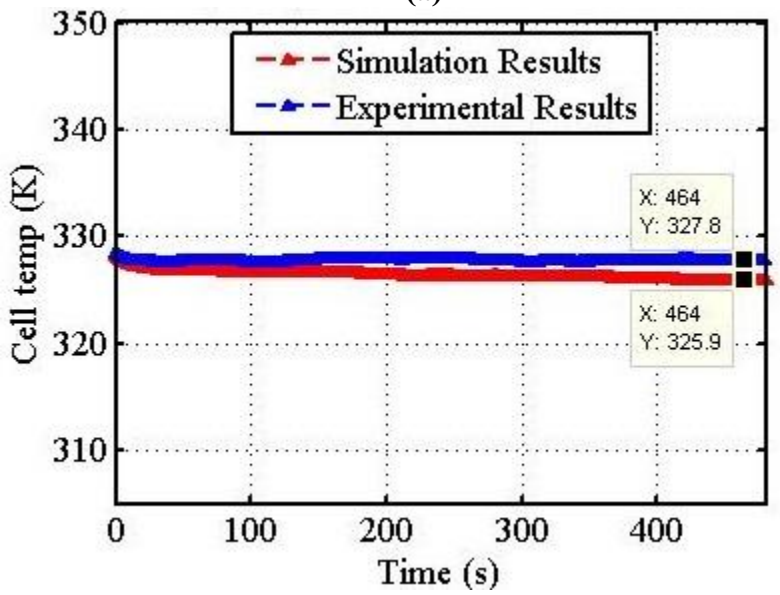

(b)

Figure 15: (a) Operating point and (b) comparison of PV cell's temperature at G= 1060W/m^2 when output voltage is held at 0.4V.

4.2.4 Fixed PV Current Operation

The thermal model in Simulink is examined under 960 W/m^2 irradiance and the operating point is fixed at a constant current of 1.9 A with 303 K ambient temperature. The simulation is run under the same conditions for 480 sec, and cell temperature results are compared in Fig. 16. As shown, the average simulation cell temperature is 324.6 K, which is close to the results from the experiment of 325.7 K. The simulation data follows the trend of measured data closely, with only 1.27% error.

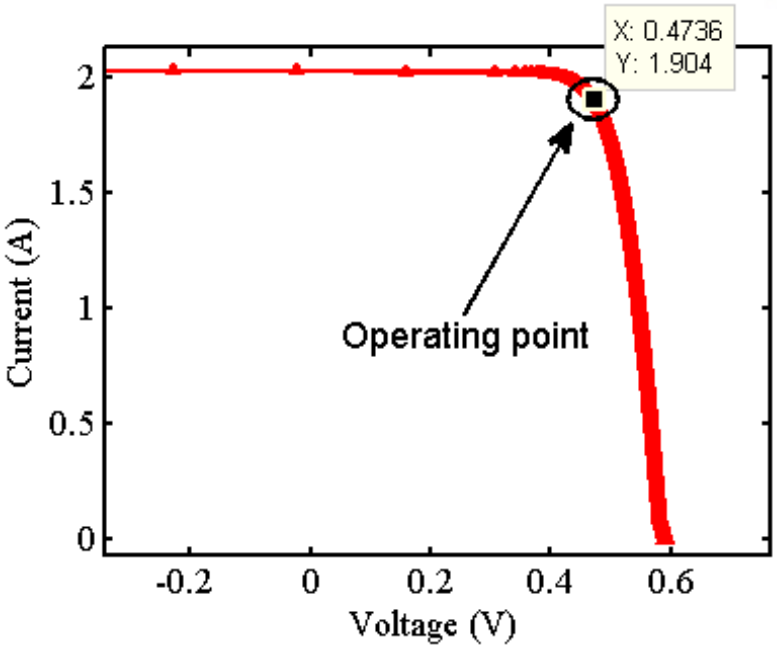

(a)

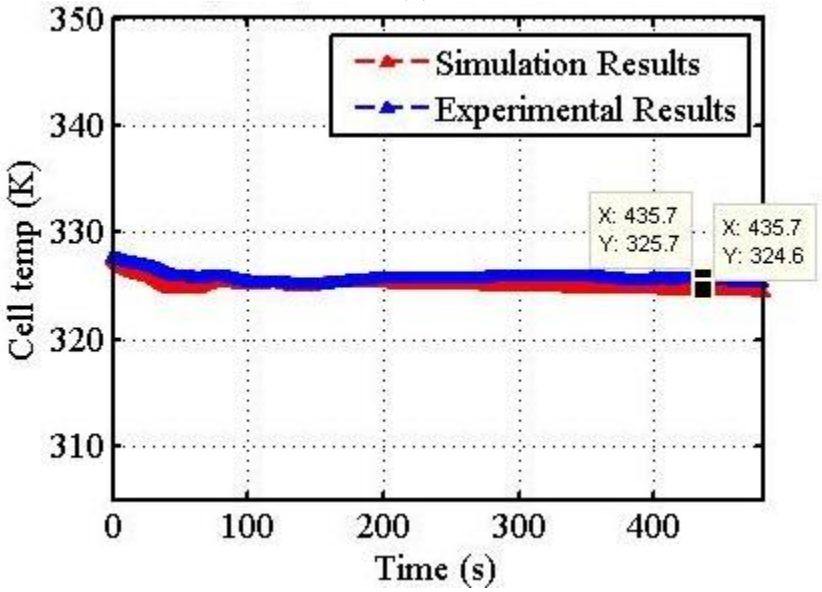

(b)

Figure 16: (a) Operating point and (b) comparison of PV cell's temperature at G=960W/m^2 when input current is held at 1.9 A

4.3 Dynamic Condition Verification using PHILS

Here, the electric-thermal PV model is used with the PHILS setup to test its dynamic performance. First, a step load variation test is conducted to examine the PHILS system dynamic characteristics. Then, a MPPT test case is conducted, where the PV current is set to emulate the operation of a PV connected power converter which integrate MPPT function. For these tests, the PHILS results are compared with experimental data measured from the 1.3-W PV cell.

4.3.1 Load Step Test

In the PHILS system, there are delays from the simulation time step, dynamics of the programmable DC power supply, and the feedback current measurement. These delays can potentially affect the dynamic characteristics of the PHILS system. To determine the level of impact that these delays have on the accuracy of the PHILS system, a load step test was conducted on the experimental PV cell and on the PV model emulated with the PHILS system. Fig. 17(a) shows the step and ramp changes of the output load current, which consists of a full step up, full step down, two half steps up, and a ramp down sequence for the PV operating range of 0.1 A to 2.0 A over 70 sec. Fig. 17(b) shows the dynamic response of the output voltage for the experimental and PHILS results. There is an inherent response delay after the large load steps based on the simulation step time, but the PHILS results closely match the experimental results with no observable overshoot. The measured voltage of the PV panel is slightly lower than that of the PHILS system, with an error of 1.86%. This error stems from some modeling error combined with communication delay and inherent offset from the limited resolution of the equipment and sensors used in the PHILS setup, but is still within an acceptable range for most applications.

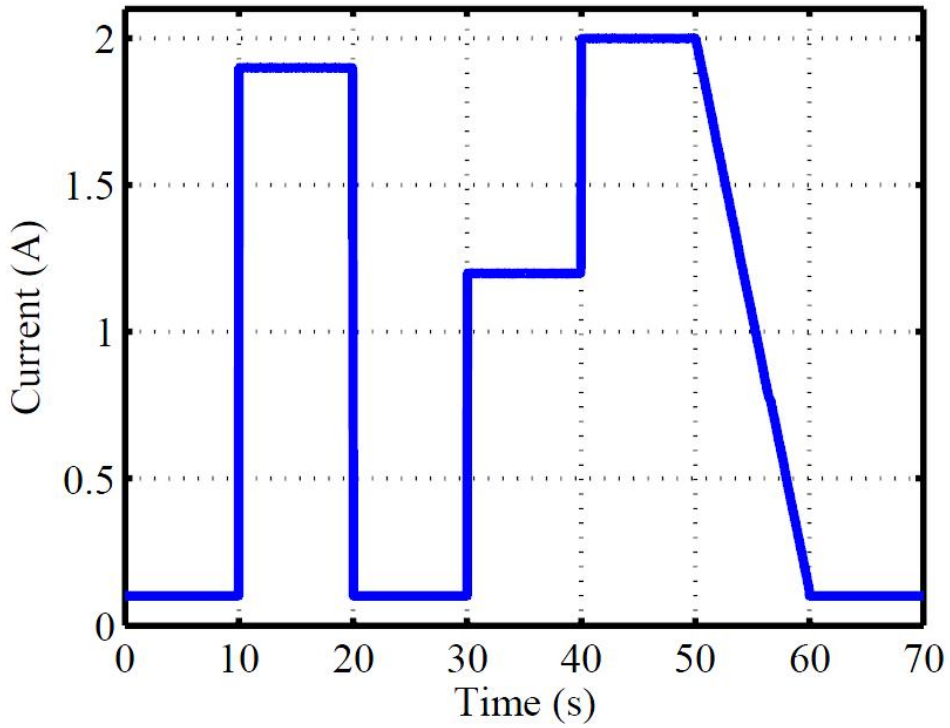

(a)

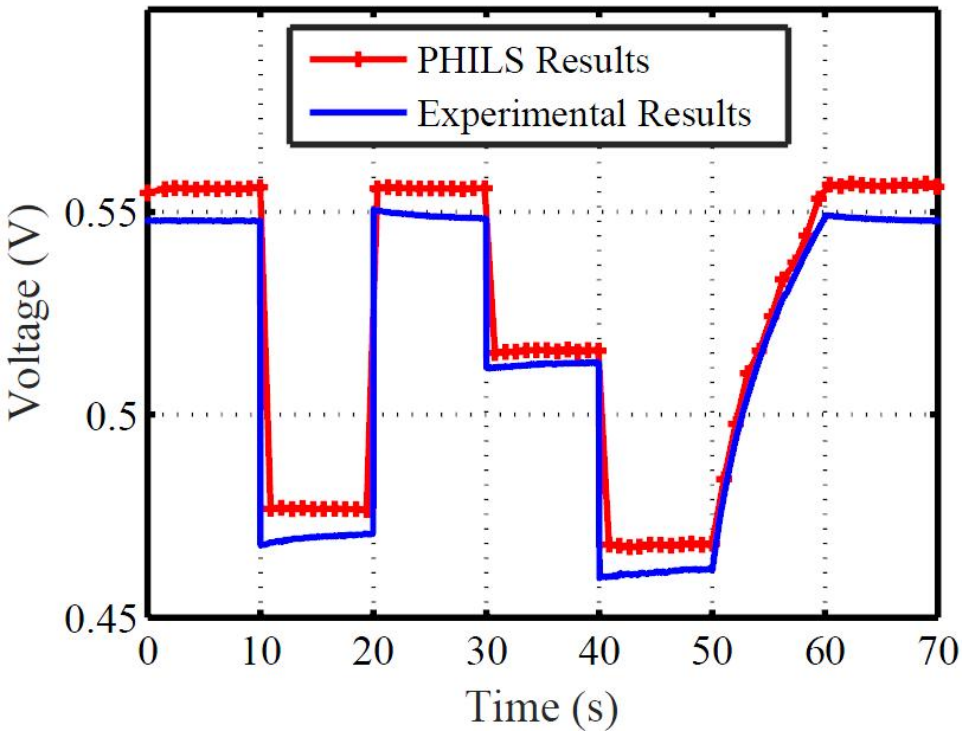

(b)

Figure 17: PV cell (a) output current load change profile and (b) dynamic comparison of the PHILS and experimental voltage results

4.3.2 MPPT test

Next, the PHILS system is used for a MPPT test to emulate a PV cell and connect to a power converter with MPPT function integrated. The current starts from 1.20 A and ramps up to 2.28 A for the first 18 seconds; it then shown a triangular waveform that ranges from 2.22 to 2.28 A to emulate the MPPT current waveform of a DC-DC converter. The total test duration is 180 seconds and ambient temperature is 308 K.

Fig. 18(a) shows the voltage results for the measured data and PHILS system. The voltage decreases steadily for the first 18 seconds due to the increasing PV current. Then, the voltage maintains an average value around 0.44 V. Although there is a slight offset due to the previously mentioned model and equipment error, the dynamic performance of the PHILS system is well matched to the measured experimental results. The error is within 2.36% which is sufficiently high accuracy for many applications. Fig. 18(b) compares the cell temperature measured in the experiment and calculated in the PHILS model, showing that the temperature results are well matched. The maximum error is at t = 100 sec, where the model is 0.6 K lower than the measured cell temperature. Overall, the error is within 0.19% for the 3-minute test. These results show that the electric-thermal model implemented in PHILS accurately calculates and emulates the PV cell's operating characteristics in realistic test conditions.

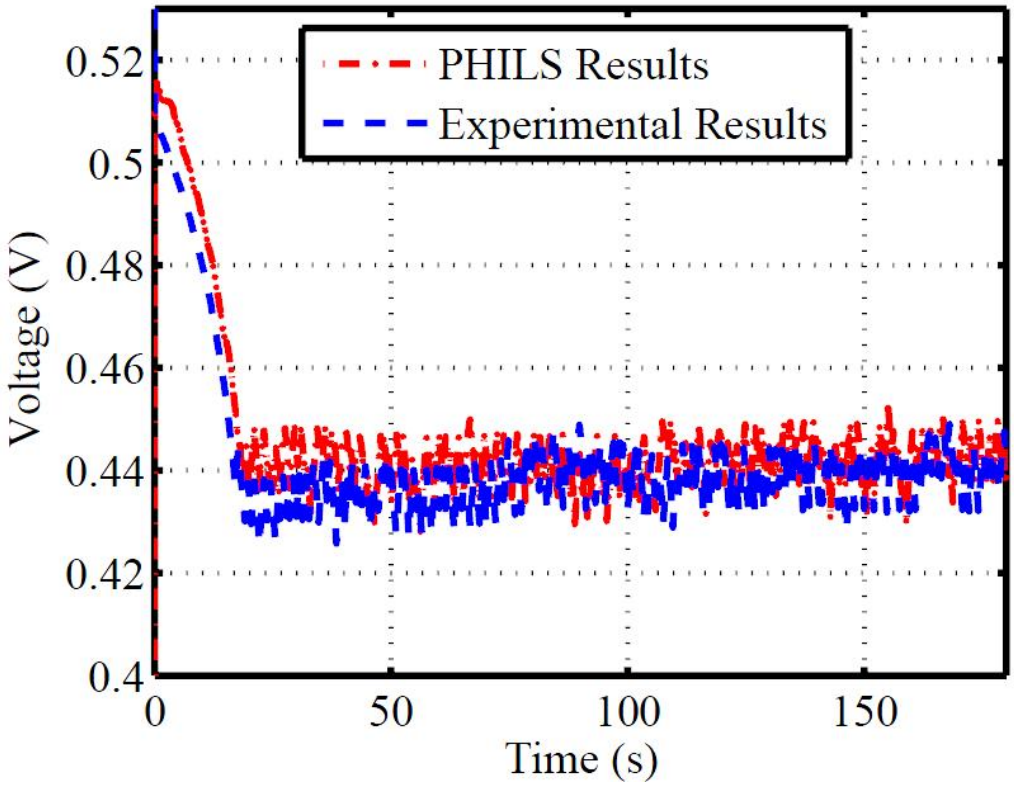

(a)

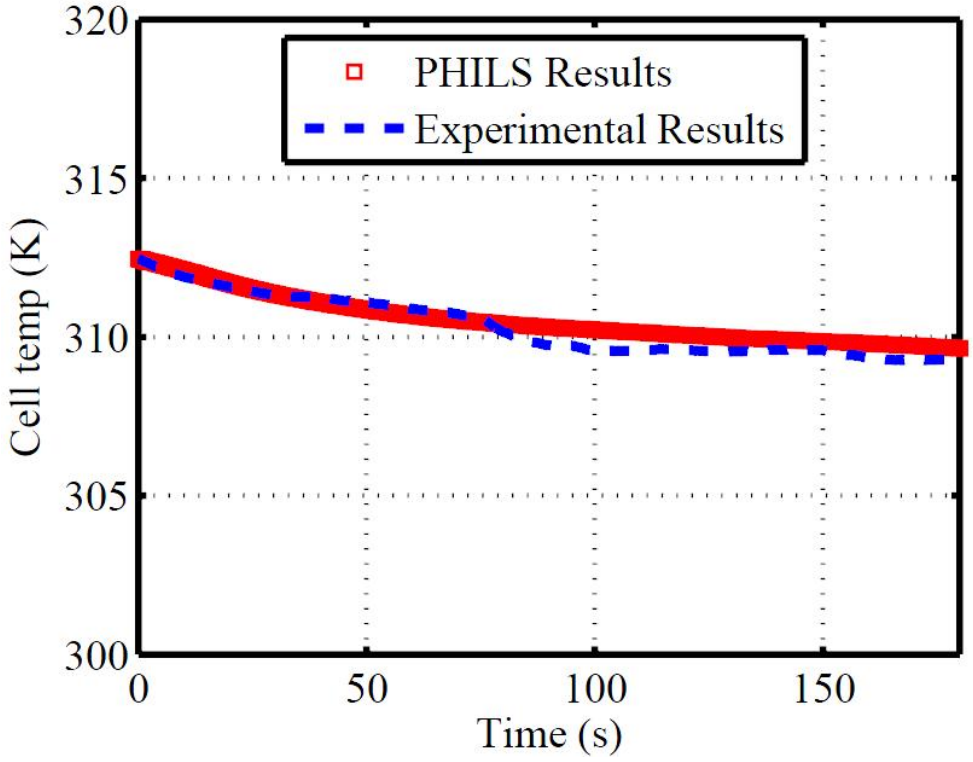

(b)

Figure 18: Comparison of the PV cell's (a) operating voltage and (b) cell temperature with irradiance at 1077 to 110 W/m^2 and current varying from 1.2 to 2.32 A.

CHAPTER 5
DISCUSSION

Based on the static and dynamic tests, the electric-thermal PV model can emulate real solar cells in various operating conditions. The model's electrical aspects show high accuracy with error within 1.18% for the static condition, 1.86% for the load step, and 2.36% for the realistic operation test. The temperature was within an error of 1.48% for the static condition and 0.19% for the realistic operation test. In PHILS operation, the PV model proved to be comprehensive, while the calculations were fast enough to run properly in real time, without over-running during simulations. The MPPT operation test demonstrated accurate and fast dynamic performance of the model while operating in real time with the PHILS setup. The performance shown in these tests is acceptable for most PV applications that are connected to hardware, where dynamic performance is critical and trends of the electrical characteristics are more important than exact values.

The positive and advantages of this model is the feasibility to measure PV temperature while updating the electrical characteristics of the PV to increase efficiency. Due to this comprehensive approach, the model is eligible for operating in real time with the Power-Hardware-in-the-Loop technique and hence, enabling the ability to interface with real power hardware converter with other integrated functions such as MPPT or fault detection. The model also features fast settling time which is also important when operating in fast changing condition.

Due to the above feature, this model can be utilized in various applications. The most notable one is the capability to analyze and manage large PV system without the need for costly setup with complex operation. Testing multiple PV panels operation with power converter is also feasible with the help of fast and accurate characteristics of the model. Another application is to examine MPPT functionality in an easy way without having to rely on real PV system or weather condition, a factor that is always a challenge for PV related-field. Also, thanks to the ability to manage PV temperature, fault detection can be improved and make the process to locate damaged PV cells faster. The inequality in a batch of PV panel could also indicate susceptible cells when shading occurs in the system.

Although covering the temperature aspect of PV, this model has yet to distinguish between unity heating and partial heating. As an example in Figure 19, the PV cell is experiencing second breakdown, an effect which make part of the cell to heat up dramatically which is called hot spotting.

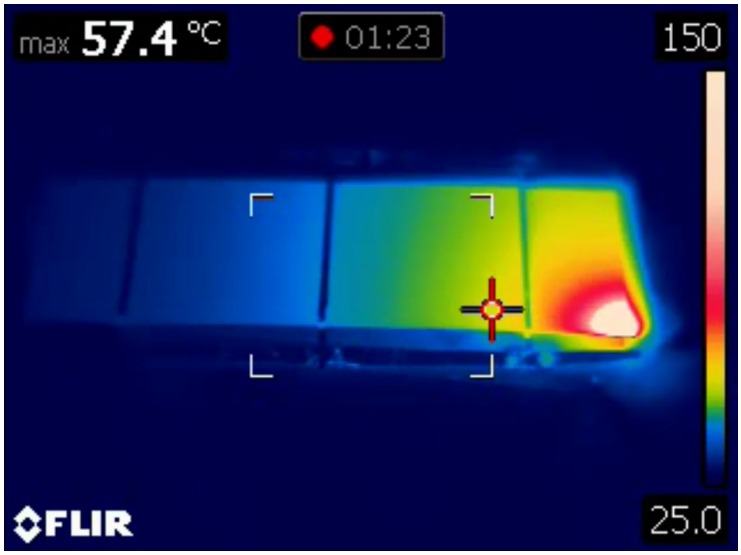

Figure 19: Thermal image of a PV cell experiencing hot spotting

As shown, the corner of the cell can go up to 150 degree Celsius but in the model, these kind of phenomenon has yet to be accounted for and will be an improvement for future update. As mentioned before, second breakdown is a fault in PV operation which make the affected PV's I-V curve to be alternated. Figure 20 shows the I-V curve of a PV cell which has fallen in to second breakdown, whenever the PV operating voltage reaches the first breakdown voltage, it will bend in a reversed direction, increasing in value and in the end moving asymptotically with the 0 V line. Future improvement to the model will account for this effect which could be more helpful for fault detection applications

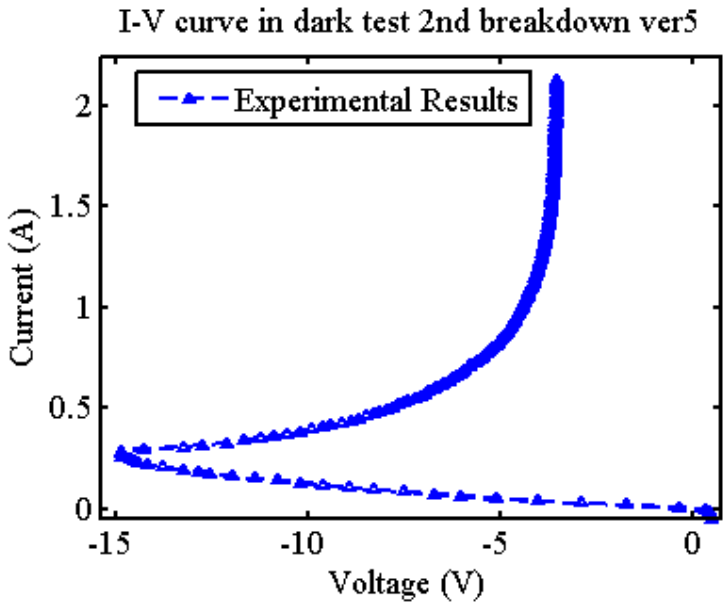

Figure 20: I-V curve of a PV cell affected by second breakdown

CHAPTER 6
CONCLUSION

Real-time simulation is a convenient and cost effective way to test and emulate PV systems. For these emulated system to be accurate, PV models must be comprehensive enough to model reverse-bias, dynamic, and thermal characteristics, while being simple enough to be calculated in real time. The proposed dynamic electric-thermal PV model was developed and fully defined in (1) to (24). An experimental and PHILS setup was built to validate the electrical and thermal aspect of the model through static and dynamic condition testing. In the static condition test, multiple I-V sweep tests showed that the electrical and thermal aspects of the model were well matched with error within 1.18% and 1.48%, respectively. The dynamic condition tests were run in real-time with the PHILS setup. The load step verifies acceptable dynamic performance with only a small delay and an overall error of 1.86%. The realistic operation test emulated a PV cell interfacing with a power converter, which showed error within 2.36% for the electrical characteristics and error within 0.19% for the thermal characteristics. These results prove the feasibility of the proposed electric-thermal PV model working through PHILS to interface with physical hardware.

The major contributions of this paper are as follows: 1) integrating a comprehensive PV model with a thermal model to develop a model that can accurately calculate cell I-V characteristics and temperature, 2) developing a custom setup to precisely measure temperature at the solar cell and glass surfaces by introducing a five-layer thermal model to validate the thermal model, 3) successfully adapting electric-thermal model to work in PHILS, 4) verifying the accuracy of the model and its ability interface with power converter hardware in real-time with PHILS. Ultimately, this model can be used to accurately model crystalline PV cells or panels in real-time operation to emulate a wide range of applications.

REFERENCES

[1] M. A. Ramli, E. Prasetyono, R. W. Wicaksana, N. A. Windarko, K. Sedraoui, and Y. A. Al-Turki, "On the investigation of photovoltaic output power reduction due to dust accumulation and weather conditions," Renewable Energy, vol. 99, pp. 836–844, 2016.

[2] H. Sridhar and K. S. Meera, "Study of grid connected solar photovoltaic system using real time digital simulator," in Int. Conf. on Advances in Electronics, Computers and Communications, Oct. 2014, pp. 1–6.

[3] D. S. Karanjkar, S. Chatterji, S. S. L., and A. Kumar, "Real time simulation and analysis of maximum power point tracking (mppt) techniques for solar photo-voltaic system," in Recent Advances in Engineering and Computational Sciences, Mar. 2014, pp. 1–6.

[4] O. Nzimako and R. Wierckx, "Modeling and simulation of a grid integrated photovoltaic system using a real-time digital simulator," in Clemson University Power Systems Conference, Mar. 2015, pp. 1–8.

[5] Y. Yadav, R. Roshan, S. Umashankar, D. Vijayakumar, and D. P. Kothari, "Real time simulation of solar photovoltaic module using labview data acquisition card," in Int. Conf. on Energy Efficient Technologies for Sustainability, Apr. 2013, pp. 512–523.

[6] J. Khazaei, L. Piyasinghe, Z. Miao, and L. Fan, "Real-time digital simulation modeling of single-phase pv in rt-lab," in 2014 IEEE PES General Meeting, July 2014, pp. 1–5.

[7] J.-H. Jung and S. Ahmed, "Real-time simulation model development of single crystalline photovoltaic panels using fast computation methods," Solar Energy, vol. 86, no. 6, pp. 1826–1837, 2012.

[8] J.-H. Jung, "Power hardware-in-the-loop simulation (phils) of photovoltaic power generation using real-time simulation techniques and power interfaces," J. of Power Sources, vol. 285, pp. 137–145, 2015.

[9] S. Cannizzaro, M. C. D. Piazza, M. Luna, and G. Vitale, "Generalized classification of pv modules by simplified single-diode models," in IEEE Int. Symposium on Industrial Electronics, June 2014, pp. 2266–2273.

[10] E. I. Batzelis and S. A. Papathanassiou, "A method for the analytical extraction of the single-diode pv model parameters," IEEE Transactions on Sustainable Energy, vol. 7, no.2, pp. 504–512, Apr. 2016.

[11] S. Shongwe and M. Hanif, "Comparative analysis of different single-diode pv modeling methods," IEEE J. Photovolt., vol. 5, no. 3, pp. 938–946, May 2015.

[12] E. I. Batzelis, G. E. Kampitsis, S. A. Papathanassiou, and S. N. Manias, "Direct mpp calculation in terms of the single-diode pv model parameters," IEEE Trans. Energy Convers., vol. 30, no. 1, pp. 226–236, Mar. 2015.

[13] M. G. Villalva, J. R. Gazoli, and E. R. Filho, "Comprehensive approach to modeling and simulation of photovoltaic arrays," IEEE Trans. Power Electron., vol. 24, no. 5, pp. 1198–

1208, May 2009.

[14] K. A. Kim, C. Xu, J. Lei, and P. T. Krein, "Dynamic photovoltaic model incorporating capacitive and reverse-bias characteristics," IEEE J. Photovoltaics, vol. 3, no. 14, pp. 1334–1341, 2013.

[15] K. A. Kim, G. S. Seo, B. H. Cho, and P. T. Krein, "Photovoltaic hot-spot detection for solar panel substrings using ac parameter characterization," IEEE Trans. Power Electron., vol. 31, no. 2, pp. 1121–1130, Feb. 2016.

[16] K. A. Kim and P. T. Krein, "Photovoltaic hot spot analysis for cells with various reverse-bias characteristics through electrical and thermal simulation," in Proc. IEEE Workshop Control Modeling Power Electron., June 2013, pp. 1–8.

[17] A. Jones and C. Underwood, "A thermal model for photovoltaic systems," Solar Energy, vol. 70, no. 4, pp. 349 – 359, 2001.

[18] H. Bounechba, A. Bouzid, H. Snani, and A. Lashab, "Real time simulation of mppt algorithms for pv energy system," Int. J. of Electrical Power and Energy Systems, vol. 83, pp. 67–78, 2016.

[19] O. Nzimako and R. Wierckx, "Stability and accuracy evaluation of a power hardware in the loop (phil) interface with a photovoltaic micro-inverter," in Annual Conference of the IEEE Industrial Electronics Society, Nov. 2015, pp. 5285–5291.

[20] Solar and HelioSpheric Observatory. (2016, Dec 31). *Our Star the Sun* [Online]. Available: https://soho.nascom.nasa.gov/explore/

[21] The Sun Today: Solar facts and Space weather. (2016, Dec 31). *The Sun* [Online]. Available: http://www.thesuntoday.org/the-sun/

[22] Solar Energy. (2016, Dec 31). *From Sun to Earth* [Online]. Available: http://almashriq.hiof.no/lebanon/600/610/614/solar-water/unesco/21-23.html

[23] Seeding Socioeconomic Avalanches. (2016, Dec 31). *Earth's Energy Budget* [Online]. https://edro.wordpress.com/energy/earths-energy-budget/

[24] Sunipod: Independently Happy. (2016, Dec 31). *Photovoltaic Cells* [Online]. Available: http://www.sunipod.com/photovoltaic-cells.php

[25] T. Douglas, "Dynamic modelling and simulation of a solar-pv hybrid battery and hydrogen energy storage system," J. of Energy Storage, vol. 7, pp. 104–114, 2016.

[26] M. Antonelli, A. Baccioli, M. Francesconi, and U. Desideri, "Dynamic modelling of a low-concentration solar power plant: A control strategy to improve flexibility," Renewable Energy, vol. 95, pp. 574 – 585, 2016.

[27] L. Weili, Z. Yu, and C. Yuhong, "Calculation and analysis of heat transfer coefficients and temperature fields of air-cooled large hydro-generator rotor excitation windings," IEEE Transactions on Energy Conversion, vol. 26, no. 3, pp. 946–952, Sept. 2011.

[28] Y. Luo, L. Zhang, Z. Liu, Y. Wang, F. Meng, and J. Wu, "Thermal performance evaluation of an active building integrated photovoltaic thermoelectric wall system," Applied Energy, vol. 177, pp. 25 – 39, 2016.

[29] S. Vergura, G. Acciani, and O. Falcone, "A finite-element approach to analyze the thermal effect of defects on silicon-based pv cells," IEEE Transactions on Industrial Electronics, vol. 59, no. 10, pp. 3860–3867, Oct. 2012.

[30] A. J. Veldhuis, A. M. Nobre, I. M. Peters, T. Reindl, R. Rther, and A. H. M. E. Reinders, "An empirical model for rack-mounted pv module temperatures for southeast asian locations evaluated for minute time scales," IEEE J. Photovolt., vol. 5, no. 3, pp. 774–782, May 2015.

[31] M. D. Perez and N. E. Gorji, "Modeling of temperature profile, thermal runaway and hot spot in thin film solar cells," Materials Science in Semiconductor Processing, vol. 41, pp. 529 – 534, 2016.

[32] N. N. Afiqah, H. A. Hamid, A. N. Syafawati, and M. Irwanto, "Building integrated photovoltaic: Analysis of wind effect due to convection heat transfer," in IEEE Int. Conf. on Control System, Computing and Engineering, Nov. 2015, pp. 91–95.

[33] J. Nou, R. Chauvin, S. Thil, and S. Grieu, "A new approach to the real-time assessment of the clear-sky direct normal irradiance," Applied Mathematical Modelling, vol. 40, no. 1516, pp. 7245–7264, 2016.

[34] M. Hejri, H. Mokhtari, M. R. Azizian, M. Ghandhari, and L. Sder, "On the parameter extraction of a five-parameter double-diode model of photovoltaic cells and modules," IEEE Journal of Photovoltaics, vol. 4, no. 3, pp. 915–923, May 2014.

[35] R. J. Serna, B. J. Pierquet, J. Santiago, and R. C. N. Pilawa-Podgurski, "Field measurements of transient effects in photovoltaic panels and its importance in the design of maximum power point trackers," in IEEE Applied Power Electronics Conf. and Exposition, Mar. 2013, pp. 3005–3010.

[36] H. Zheng, "Solar photovoltaic energy generation and conversion from devices to grid integration," Dissertation for Doctor of Philosophy, pp. 6–8, 2013.

[37] C. Alex Young. (2016, Dec 11). *How Big is the Sun?* [Online]. Available: http://www.thesuntoday.org/solar-facts/how-big-is-the-sun/

[38] Precipitation Education. (2016, Dec 11). *Global Energy budget* [Online]. Available: https://pmm.nasa.gov/education/lesson-plans/global-energy-budget

[39] Gil Knier. (2016, Dec 11). *How do Photovoltaic work?* [Online]. Available: https://science.nasa.gov/science-news/science-at-nasa/2002/solarcells

[40] SNDNSHR (2016, Dec 11). *What is Maximum Power Point Tracking* [Online]. Available: https://sndnshrblog.wordpress.com/2015/11/29/what-is-maximum-power-point-tracking/

[41] Seyed Mehdi Mohaghegh. (2016, Dec 11). *CSP vs PV – Understanding the current situation and future outlook* [Online]. Available: https://blogs.ucl.ac.uk/sustainable-

resources/2015/11/30/csp-vs-pv-understanding-the-current-situation-and-future-outlook/

[42] Energy without Carbon. (2016, Dec 11). *Concentrator Dish PV* [Online]. Available: http://www.energy-without-carbon.org/ConcentratorDishPV

[43] NASA. (2016, Dec 11). *Low-Cost, Rugged, High-Efficiency Solar Cell* [Online]. Available: https://technology.nasa.gov/patent/LEW-TOPS-50

ACKNOWLEDGMENT

This work was supported by the 1.160085.01 Project Research Fund at the Ulsan National Institute of Science and Technology (UNIST). Special thanks to Prof. Katherine A. Kim for advising this research and editorial help on this thesis, Prof. JeeHoon Jung for advising this research and real time simulations, Hyunji Lee, Kwon KyongJun, Cho Hyuntae and other members of PEARS Lab for their help and collaboration, Kwak SangKyu for helping me on Power Hardware in the Loops simulations and to my family and friends for their encouragement and support.